



Wake structure of an array of cylinders in shallow flow

Fei He^{1,†}, Marco Ghisalberti^{1,2,†}, Hongwei An¹, Scott Draper^{1,2}, Paul Branson^{2,3}, Chengjiao Ren¹ and Liang Cheng^{1,4}

¹School of Engineering, The University of Western Australia, 35 Stirling Highway, Crawley, WA 6009, Australia

²Oceans Graduate School, The University of Western Australia, 35 Stirling Highway, Crawley, WA 6009, Australia

³Environment, CSIRO, 35 Stirling Highway, Crawley, WA 6009, Australia

⁴Guangzhou International Campus, South China University of Technology, Guangzhou, 511442, PR China

(Received 11 September 2023; revised 8 February 2024; accepted 23 March 2024)

Although there is a range of approaches for classifying the wake structure behind an array of obstacles, these approaches provide inconsistent results across different array systems. This motivates the present study to integrate and reconcile these approaches into one that is consistent across different systems. This new, transferable classification approach is based on the dimensionless flow blockage of the array and the wake stability parameter. To demonstrate this approach, a series of laboratory experiments was conducted to characterise the wake structure behind an array of emergent cylinders across a practically relevant parameter space that has not previously been explored. Two arrays with the same values of flow blockage and wake stability parameters but different sizes display the same wake structure, demonstrating the controlling influence of these two parameters on the wake structure. This approach classifies four different wake structures, which are distinct in that they display differences in instantaneous and time-averaged flow fields, temporal velocity oscillations, shear layer growth and the length of the steady wake region. The dependence of the wake structure on the two parameters is a consequence of (i) the controlling influence of blockage on the fraction of incident flow passing through the array and (ii) the ability of shallowness to suppress wake instabilities and, to a lesser extent, also influence the velocity through the array. This paper provides a predictive framework for the wake structure based on knowledge of the array geometry, and the depth and velocity of incident flow across the entire relevant practical parameter space.

Key words: wakes, flow–structure interactions, shallow water flows

† Email addresses for correspondence: fei.he@research.uwa.edu.au, marco.ghisalberti@uwa.edu.au

© The Author(s), 2024. Published by Cambridge University Press. This is an Open Access article, distributed under the terms of the Creative Commons Attribution licence (<http://creativecommons.org/licenses/by/4.0/>), which permits unrestricted re-use, distribution and reproduction, provided the original article is properly cited.

1. Introduction

Shallow flows through arrays of obstacles are ubiquitous in natural and engineered systems, such as flows through patches of aquatic vegetation (Chen *et al.* 2012), groups of bridge piers (Sumer & Fredsøe 1997), pile foundations (Ball *et al.* 1996; Coulbourn *et al.* 2011) and arrays of tidal stream turbines (Creed *et al.* 2017). Drag on an obstacle array creates a region of low momentum fluid immediately downstream (the wake). Depending on the balance of forces in the wake, the wake can take a variety of different forms. To first approximation, these obstacle arrays can be modelled by a circular array of cylinders, which allows for studying fundamental fluid mechanics of wake structure relevant to practical applications. The wake structure controls the transport of mass and momentum behind these arrays (e.g. Follett & Nepf 2012; Zong & Nepf 2012).

Taking flow through a patch of aquatic vegetation as a canonical example, the wake structure was shown to have significant ecological and geomorphological implications. The wake structure has been demonstrated to control the morphology of mobile bed sediments in the lee of aquatic vegetation. Wakes with a von Kármán vortex street were observed to spread sediment towards the wake centreline, whilst wakes without the vortex street spread sediment away from the wake centreline (Follett & Nepf 2012). Flow passing through the vegetation patch can generate a steady flow region immediately behind the patch with relatively low velocity and turbulence levels (Zong & Nepf 2012), such that sediment erosion is reduced and fine particle deposition is elevated in the region (Chen *et al.* 2012). The steady wake region, whose scale can vary widely with flow and vegetation characteristics, is therefore a suitable site for the establishment of seeds and is favourable for new plant growth by providing a stable substrate (Follett & Nepf 2012). Because of this, vegetation patches in channels have been found to propagate predominantly in the downstream direction, forming a streamlined shape extensively observed in the field (Duarte & Sand-Jensen 1990; Gurnell *et al.* 2001). These practical implications highlight the importance of understanding the wake structure in shallow flow, in particular if prediction of the wake structure can inform the design of vegetation restoration projects.

A range of parameters has been proposed for classification of wake structure behind an array of cylinders in vertically unbounded flow (without bed). These parameters include the gap ratio G/d (where G is the centre-to-centre distance between the nearest tandem cylinders in a staggered array and d is the cylinder diameter) (Ball *et al.* 1996; Takemura & Tanaka 2007) and the solid volume fraction ($\phi = (\pi/4)nd^2$, where n is the number of cylinders per unit area) (Nicolle & Eames 2011; Zong & Nepf 2012). These two geometric parameters describe the local cylinder configuration within the array but without considering the influence of the array size D/d defined by Chang & Constantinescu (2015) (D is the array diameter).

By varying these geometric parameters, three different wake regimes have been identified (Nicolle & Eames 2011; Zong & Nepf 2012): (i) coupled individual wake (CI), in which the array wake is dominated by individual wakes of the cylinders making up the array; (ii) ‘steady + shedding’ wake (SS), in which a steady wake region occurs behind the array, followed downstream by a von Kármán vortex street; and (iii) vortex street wake (VS), in which a von Kármán vortex street forms immediately behind the array. However, some flows reported in literature cannot be classified into these three regimes. Whilst these unclassified flows do not exhibit a von Kármán vortex street, the array shear layers are unstable with large-scale undulatory motions (Zong & Nepf 2012; Chang & Constantinescu 2015). It appears that these cases might fall into a fourth regime that requires further investigation, which is one of the motivations for the present work.

The critical values of solid volume fraction and gap ratio defining the same wake transition are inconsistent across different systems. For instance, it was shown by Nicolle

& Eames (2011) that the wake transits from regime CI to SS and to VS at $\phi = 0.05$ and 0.15 , respectively. In contrast, the wake transition from regime CI to SS was found in the range of $\phi = 0.05\text{--}0.1$ by Chang & Constantinescu (2015) and at $\phi = 0.04$ by Zong & Nepf (2012). Similarly, wake transition from CI and SS occurred in the range of $G/d = 1\text{--}2$ reported by Takemura & Tanaka (2007) and distinctly at $G/d > 8$ reported by Ball *et al.* (1996). These critical G/d values correspond to $\phi = 0.23\text{--}0.91$ for Takemura & Tanaka (2007) and $\phi > 0.01$ for Ball *et al.* (1996) (taking $\phi = (\sqrt{3}\pi/6)d^2/G^2$ for their staggered arrays). The difference in the threshold of the same wake transition between different studies indicates that neither ϕ nor G/d completely defines the wake structure.

Physically, in vertically unbounded flow, the wake structure behind an array of cylinders depends on the velocity of bleeding flow due to the stabilisation effect of bleeding flow on the wake (Nicolle & Eames 2011). This bleeding velocity has been shown to be a function of the dimensionless flow blockage parameter (Chang & Constantinescu 2015):

$$\Gamma_D = \frac{C_d a D}{(1 - \phi)}, \quad (1.1)$$

where $a = nd$ is the frontal area of cylinders within the array per volume, D is the array diameter and C_d is the average drag coefficient of individual cylinders, defined as

$$C_d = \frac{F}{\frac{1}{2}\rho N d \langle \bar{u} \rangle_d^2}, \quad (1.2)$$

in which F is the total drag force acting on cylinders per unit depth, $\langle \bar{u} \rangle_d$ is the spatial average of velocities over the domain occupied by fluids in the array (Eames, Hunt & Belcher 2004), ρ is the fluid density and N is the total number of cylinders within the array. This parameter represents the scaling ratio of two terms in the streamwise momentum equation: the drag on the array elements retarding the flow and the streamwise advection term describing flow deceleration through the array (Rominger & Nepf 2011). Importantly, it is seen that Γ_D , defining the blockage of an array to flow, is not only dependent on ϕ but is also governed by C_d and the dimensionless array size D/d ((1.1) can be re-written as $\Gamma_D = (4C_d/\pi)(\phi/(1 - \phi))(D/d)$). The incompleteness of using G/d and ϕ to define the array-induced flow blockage may explain the inconsistency in existing wake classification approaches based on G/d and ϕ . The flow blockage parameter has been used to describe the bleeding flow through a submerged cylinder array by Belcher, Jerram & Hunt (2003), an infinitely long array of cylinders by Rominger & Nepf (2011) and a finite, circular array by Chang & Constantinescu (2015). However, the influence of Γ_D on wake structure behind a cylinder array has not been investigated yet.

When the water depth is small relative to the horizontal scale of the array ('shallow'), flow shallowness is also physically important in controlling wake structure. The effect of flow shallowness is not well understood for an array of cylinders but it has been explored in more detail for an isolated solid cylinder (for which $\phi = 1$, $\Gamma_D = \infty$). The shallowness influences the wake development behind an isolated cylinder in two ways (Chen & Jirka 1995): (i) it restricts spanwise motions such that the wake structure is largely two-dimensional; and (ii) bed friction acts to suppress the transverse motion of large-scale disturbances such as vortex shedding.

The shallowness effects on the wake structure behind the isolated cylinder can be described by the wake stability parameter:

$$S_C = \frac{C_f D}{h}, \quad (1.3)$$

where C_f is the bed friction coefficient and h is the water depth (Ingram & Chu 1987). This parameter represents the scaling ratio between the energy production from the mean shear and energy dissipation by bed friction in the turbulent kinetic energy equation (Chu, Wu & Khayat 1991). Hence, it is a measure of the stabilising influence of bed friction relative to the destabilising influence of transverse shear on the development of wake instabilities downstream of the isolated cylinder.

Extending this wake stability parameter to an array of cylinders is, however, not limited to only quantifying the shallowness influences on wake development downstream of the array because it may also describe the shallowness effect on the bleeding flow that stabilises the wake. For a cylinder array, this wake stability parameter also represents the scaling ratio between the bed friction term and the inertial term in the streamwise momentum equation for the flow diverted around the array (termed ‘diverted flow’) (White & Nepf 2007). The bed friction has been shown to impede the faster diverted flow, which in turn increases the velocity of bleeding flow (Creed *et al.* 2017). The increased bleeding velocity will lead to a more stabilised wake (Nicolle & Eames 2011). Despite being implied by the energy and momentum conservation, the combined influence of S_C on wake structure of an array of cylinders has not been experimentally explored and confirmed.

The wake structure behind an isolated cylinder was found to be solely controlled by wake stability parameter when the depth Reynolds number (where $Re_h = U_\infty h/\nu$ in which ν is the kinematic viscosity and U_∞ is velocity upstream of the obstacle) is higher than 1500 (Chen & Jirka 1995). However, this is not the case for an array of cylinders. The wake stability parameter basically is a relative measure of strength of the transverse shear to the bed shear. For an isolated cylinder, the strength of transverse shear scales on the body diameter D (Ingram & Chu 1987) that is incorporated in S_C . In contrast, for an array of cylinders, the transverse shear strength is determined by the difference between the bleeding flow and diverted flow (Chang & Constantinescu 2015). The strength is not a simple scaling relation with D but is associated with Γ_D that controls the bleeding velocity. This means that the threshold of S_C for the same wake transition should be dependent on Γ_D . Although this argument has not been confirmed by varying Γ_D systematically, it is, to some extent, supported by the observation with varying ϕ by Wang *et al.* (2019). In their study, vortex street was shown behind a cylinder array with $\phi = 0.1$ at $S_C = 0.03$ but was absent for the array with $\phi = 0.03$ at the same S_C value. Note that the two solid volume fractions correspond to two different values of flow blockage parameter ($\Gamma_D = 1.7, 4.9$).

Considering the findings described above, it is apparent that none of gap ratio, solid volume fraction and wake stability parameter independently provides a universal description about wake structure behind an array of cylinders in shallow flow. This motivates the present study to integrate and reconcile wake classification approaches into one that is consistent across different flow-array systems and different parts of the parameter space for ϕ , G/d and S_C . Applying energy and momentum conservation to the system as described above implies that the wake structure associated with shallow flow through an array of cylinders should be, to first order, controlled by both flow blockage and wake stability parameters (Γ_D , S_C). This combined parameter set contributes to a new integrated, transferable approach for wake classification.

This integrated approach will be validated by a thorough experimental exploration of wake structure across physically important flow conditions that have not been investigated before. Table 1 indicates that existing work has largely focused on flows with $S_C < 0.01$. However, the S_C value exceeds 0.01 for many systems of interest. Taking reeds in rivers and seagrasses in oceans as two archetypal examples, the typical patch widths are $D \sim O(1\text{--}100\text{ m})$, with per-volume frontal areas of $a \sim O(0.1\text{--}1\text{ m}^{-1})$ (e.g. Wang & Wang

| Previous study | Method | Parameter used for wake classification | Parameter range |
|-------------------------------|--------|--|---|
| Chen & Jirka (1995) | Exp. | S_C | $\phi = 1$ (solid), $0.03 < S_C < 0.94$ |
| Ball <i>et al.</i> (1996) | Exp. | G/d | $2 < G/d < 8$ ($0.02 < \phi < 0.29$) |
| Takemura & Tanaka (2007) | Exp. | G/d | $1.25 < G/d < 6$ ($0.04 < \phi < 0.57$) |
| Nicolle & Eames (2011) | Num. | ϕ | $0.002 < \phi < 0.30$ |
| Zong & Nepf (2012) | Exp. | ϕ | $0.03 < \phi < 0.36$ |
| Chang & Constantinescu (2015) | Num. | ϕ | $0.023 < \phi < 0.20$ |
| Kim <i>et al.</i> (2015) | Num. | ϕ | $0.03 < \phi < 0.36$ |
| Zhao <i>et al.</i> (2015) | Num. | G/d | $1.5 < G/d < 5$ ($0.04 < \phi < 0.44$) |
| Chang <i>et al.</i> (2017) | Num. | ϕ | $0.034 < \phi < 0.23$ |
| Zhang <i>et al.</i> (2019) | Num. | ϕ | $0.03 < \phi < 0.10$ |
| Wang <i>et al.</i> (2019) | Num. | ϕ, S_C | $0.03 < \phi < 0.10, 0.003 < S_C < 0.020$ |

Table 1. Summary of existing studies that investigated the wake structure behind obstacle systems. Note: Exp, laboratory experiment; Num, numerical simulation.

2007; Kotschy & Rogers 2008; Boulord *et al.* 2012). For flow depths $h \sim O(0.1-1)$ m, bed friction coefficients $C_f \sim O(0.001)$ (Ingram & Chu 1987; Nezu & Nakagawa 1993) and average drag coefficients $C_d \sim O(1)$ (Tanino & Nepf 2008; Ghisalberti 2009), the two key parameters will therefore have ranges of $S_C \sim O(0.01-0.1)$ and $\Gamma_D \sim O(0.1-100)$. Mapping out wake regimes across this practical parameter space will lead to a predictive framework for the wake structure behind an array of obstacles. Replicating existing results concerning wake structure in subsets of this parameter space will be a starting point for developing this framework.

Designing high-fidelity physical and numerical modelling studies across the full practical parameter space of Γ_D and S_C has proven challenging. In shallow water systems, the horizontal scale of the obstacle is significantly larger than the water depth. Laboratory-scale modelling of these shallow systems while keeping the channel wall blockage ratio (D/W) small enough to have negligible influence necessitates an experimental flume facility that is very wide and capable of generating flow with very small water depth (even down to 1 cm). Such flumes are not commonly available. Numerical modelling of flow through an array of cylinders in vertically unbounded flow requires resolving both the wakes of individual cylinders within the array and the wake behind the array, which is computationally demanding (He 2023). When considering shallow flow, the presence of the bottom bed imparts both dynamic (no slip) and kinematic (no flux) restrictions on the flow, resulting in a three-dimensional (3-D) flow. This bed-induced three dimensionality makes the numerical simulations of shallow flow through an array of cylinders much more computationally expensive.

Motivated by the apparent gap in existing data, together with the prevalence of shallow waters in natural and engineered systems and the need for further understanding of shallow wakes, this study explores the controlling influence of Γ_D and S_C on shallow wake structures for arrays of cylinders. By combining the present experimental results with existing work, this study aims to: (i) allow prediction of the wake regime for any given circular array of cylinders in shallow flow; (ii) understand instantaneous and time-averaged flow fields within each wake regime; and (iii) reveal the underlying physical mechanisms governing transitions between wake regimes, and their dependence upon Γ_D and S_C .

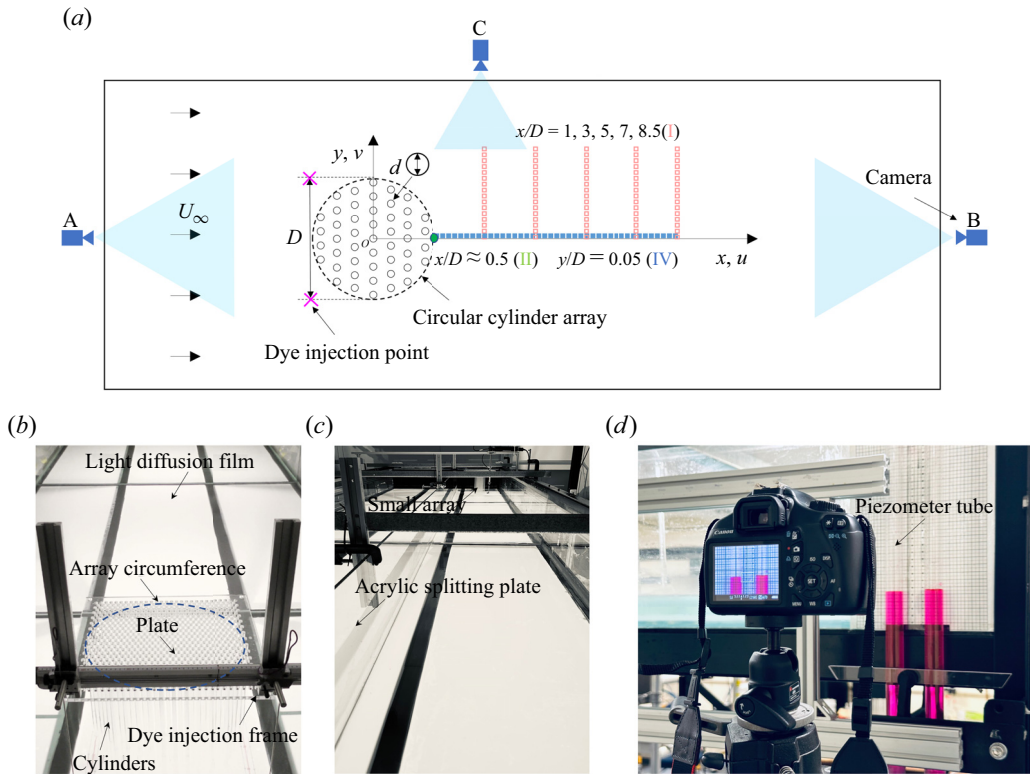


Figure 1. (a) Schematic diagram (plan view) of the experimental set-up; (b) photograph of a large array ($D=41$ cm) in the flume and dye injection system, taken by camera A; (c) photograph of a small array ($D=16$ cm) in a narrow channel created by an acrylic splitting plate; (d) photograph of the piezometer set-up. The velocity measurement locations for the transverse profiles (I, red hollow square), point sampling (II, green solid circle), streamwise profile (IV, blue solid square) described in § 2.3 are sketched in panel (a).

2. Experimental methods

2.1. Shallow flow facility and model set-up

Experiments were conducted in a recirculating glass flume with a testing section of width (W) 1.85 m, length 6.0 m and maximum depth 0.35 m (figure 1a). An array of polycarbonate flow straighteners and sponges were installed at the inlet of the flume to create uniform unidirectional incident flow.

To map out wake regimes across the practical parameter space of Γ_D and S_C , 71 large arrays of acrylic clear circular cylinders with $d=1.0$ cm and $D=42.5 \pm 1.5$ cm were tested. The cylinders were organised in a staggered arrangement and extended from the flume bed through the water surface (figure 1b). Individual cylinders were held in place by a perforated acrylic plate above the water surface. The channel blockage ratio of the flume (D/W) was approximately 22%. The ambient velocity U_∞ was maintained at 10.0 cm s^{-1} . The flow depth h ranged from 1 to 11 cm, and the depth Reynolds number Re_h ranged from 1000 to 11 000.

As wake stability parameter not only varies with the flow depth but also with the array diameter, there is a need to confirm that the classification of wake regimes based on these large arrays (with virtually constant D) is independent of the array size. To do this, the wake structure is compared between six pairs of arrays, each of which has the same values

| U_∞ (cm s ⁻¹) | h (cm) | $\Delta h/h$ | C_f (measurements) | C_f (Blasius equation) |
|----------------------------------|----------|--------------|----------------------|--------------------------|
| 10 | 2.1 | 3.8 % | 0.00821 | 0.00824 (+0.3 %) |
| 10 | 1.5 | 8.1 % | 0.00893 | 0.00896 (+0.3 %) |
| 10 | 1.0 | 19.3 % | 0.00948 | 0.00991 (+4.5 %) |

Table 2. Comparison between the measured and predicted (by Blasius equation) bed friction coefficients. Here, Δh is the frictional change in water depth over 400 cm streamwise length, and h is the depth of incident flow at the upstream end of the testing section.

of Γ_D , S_C and d but different dimensionless sizes (D/d). It will be shown in § 3.1.2 that these six pairs of cases locate near the transition boundaries between different regimes. In this comparison, to keep the channel wall ratio D/W constant, for these experiments with small arrays, an acrylic splitting plate was put in the flume to form a new channel with smaller width (see figure 1c).

The bed friction coefficient C_f embedded in S_C was estimated based on the Blasius equation $C_f = 0.056/Re_h^{0.25}$ (Chow 1959) for a smooth wall. Following Chen & Jirka (1995), the estimated values were checked by measuring fractional change in water elevation for small water depth (1–2.1 cm) with a piezometer (see figure 1d). Two piezometer tubes were installed 400 cm apart (in the streamwise direction) and 20 cm away from the channel wall to measure the frictional change across these two locations. The 400 cm length covers approximately a $10D$ wake length in this study. A fixed Canon camera was used to obtain frames of the water levels in the piezometer tubes. KeystoneTM Rhodamine dye in magenta was added into the two tubes to illuminate the water columns. The fractional change in water depth Δh (hence streamwise pressure gradient) between the two locations was calculated using image pixels. Based on momentum balance between the bed shear and the pressure gradient, the bed friction coefficient can be experimentally calculated and compared with the predictions from the Blasius equation (see table 2).

Table 2 reveals that the Blasius equation predicts C_f to within 5 % of the measured values even for the lowest water depth ($h = 1.0$ cm). This validates the use of the Blasius equation in estimating C_f across the studied range of $1.0 \leq h \leq 11.0$ cm (92 % of cases in this study are in the range of $h \geq 1.5$ cm). This is consistent with Chen & Jirka (1995), where the similar relation of Moody friction diagram was found to be valid for a water depth as low as 1.0 cm. The small depth change ratio, $\Delta h/h \leq 19.3$ %, suggests that the water depth remains virtually invariant along the wake for $h \geq 1.0$ cm. Hence, the wake stability parameter defined based on the incident flow depth is representative (to within 19.3 %) of that over the entire wake region ($0 < x < 10D$).

The average drag coefficient C_d embedded in Γ_D was estimated by the method proposed by He *et al.* (2023). Specifically, based on the knowledge of the array geometry and the depth and velocity of the incident flow, the average drag coefficient can be calculated by running an iterative solution between the actuator disc theory (Garrett & Cummins 2007) and the empirical drag model (Tanino & Nepf 2008).

2.2. Experimental methods

Flow visualisation through dye injection was used to classify wake regimes. The wake classification will be detailed in § 3.1. A dye injection system (figure 1b) was used with a mixture of KeyacidTM Rhodamine WT liquid in magenta (Keystone company, Item ID: 703-010-27), full cream milk (Brownes Dairy, Australia) and 100 % ethanol (Chem-Supply

company) that was injected as the flow tracer at two locations $(x/D, y/D) = (-0.5, \pm 0.5)$ (figure 1a). The ratio of the volume between the milk, dye and ethanol was approximately 11 : 1 : 2 to match the density of the ambient fluid. The fattiness of milk apparently retarded diffusion of the dye solution into the ambient bulk of water to stabilise the dye filaments, and at the same time, the high reflectivity of the milk particles provided high visibility. A syringe pump was used to inject the dye steadily through a needle of inner diameter equal to 0.8 mm at mid-depth, with an injection velocity matching the local mean flow velocity.

Dye streaks were recorded with three 4K Panasonic cameras at a frame rate of 25 Hz, located outside of the flume and facing inwards towards the flume (see figure 1a). Cameras A and B, facing upstream and downstream, respectively, and camera C (side-looking) provide visualisation of the near wake of the array. Due to the wide range of the array wake and limitation of facility, it is difficult to set the cameras in a top-down view while covering the whole wake. Hence, all the cameras captured the wake structure in oblique views. The resultant oblique images were transformed into plan (top-down) view images through two-dimensional perspective transformation (using inbuilt transformation functions ‘fitgeotrans’ and ‘imwarp’ in MATLAB). To obtain images that clearly defined the wake structure, light diffusion films were placed on the underside of the glass flume base, with LED white lights positioned underneath the flume to illuminate the dye through the light diffusion film (figure 1b). Markers were put on the four corners of the flume to help establish the cartesian coordinate system on the image for further statistical image analysis.

The statistical image analysis was based on the distribution of the green intensity in pixels $G(x, y)$ (in RGB colour, with a maximum of 255) in the wake. Note that, in the RGB colour system, magenta is a secondary colour, made by combining equal amounts of red and blue colours at a high intensity. In this system, magenta is the complementary colour of green, and combining green and magenta colours will create the white colour. Therefore, the dye absorbed white light over the green wavelength range in the light spectrum such that $G(x, y)$ is qualitatively representative of the local dye concentration. The temporal variation of $G(x, y)$ is indicative of the local intensity of coherent motions, which may be quantified using a coefficient of variation as

$$C_V = \frac{\sigma_G}{\mu}, \quad (2.1)$$

where σ_G is the temporal standard deviation of $G(x, y)$ and μ is the time mean of $G(x, y)$.

Videos were recorded throughout each test, but only the last 100 seconds were used for the image analysis, covering at least five array-scale vortex shedding periods. Taking case H1 as an example (table 3), σ_G sampled at $(x/D, y/D) = (3, 0)$ converged after 45 seconds such that $(\sigma_{G,t} - \sigma_{G,t+\Delta t})/\Delta t < 0.4\%$ (figure 2a), suggesting a sampling length of 100 seconds was sufficient for statistical convergence.

The evolution of dye streaks was visualised first without the array models to allow comparison with the rate of spread of dye streaks in the presence of the arrays. It was observed that the dye streaks in the empty flume largely remained parallel without merging as they advected downstream (figure 3). The lateral spreading of the dye streaks visible in figure 3 was induced by turbulent diffusion associated with background turbulence.

Velocity measurement was undertaken to help characterise each wake regime. A Sontek two-dimensional side-looking acoustic Doppler velocimeter (ADV) was used to measure the velocity components $u(t)$ and $v(t)$, at mid-depth, in the streamwise (x) and transverse (y) directions, respectively. The ADV works in water depths down to 2 cm. In shallow flow, the velocity measured at mid-depth is a good representation of the depth-average

Wake structure of an array of cylinders in shallow flow

| Case | Name | N | G/d | d (cm) | D (cm) | h (cm) | ϕ | aD | Re_h | Γ_D | Sc | Velocity measurement type | Wake regime |
|------|------|-----|-------|----------|----------|----------|--------|-------|--------|------------|------|---------------------------|-------------|
| 1 | | 40 | 6 | 1 | 43.0 | 11.0 | 0.022 | 1.36 | 11 000 | 1.39 | 0.02 | | CI |
| 2 | A1 | 40 | 6 | 1 | 43.0 | 7.0 | 0.022 | 1.36 | 7000 | 1.39 | 0.04 | I, II | CI |
| 3 | | 40 | 6 | 1 | 43.0 | 4.6 | 0.022 | 1.36 | 4600 | 1.39 | 0.06 | | CI |
| 4 | | 40 | 6 | 1 | 43.0 | 3.0 | 0.022 | 1.36 | 3000 | 1.39 | 0.11 | | CI |
| 5 | | 40 | 6 | 1 | 43.0 | 2.1 | 0.022 | 1.36 | 2100 | 1.39 | 0.17 | | CI |
| 6 | | 40 | 6 | 1 | 43.0 | 1.5 | 0.022 | 1.36 | 1500 | 1.39 | 0.26 | | CI |
| 7 | | 57 | 5 | 1 | 41.0 | 11.0 | 0.036 | 2.41 | 11 000 | 2.50 | 0.02 | | KH |
| 8 | B1 | 57 | 5 | 1 | 41.0 | 7.0 | 0.036 | 2.41 | 7000 | 2.50 | 0.04 | I, II | KH |
| 9 | B2 | 57 | 5 | 1 | 41.0 | 4.6 | 0.036 | 2.41 | 4600 | 2.50 | 0.06 | III | CI |
| 10 | B3 | 57 | 5 | 1 | 41.0 | 3.0 | 0.036 | 2.41 | 3000 | 2.50 | 0.10 | III | CI |
| 11 | | 57 | 5 | 1 | 41.0 | 2.1 | 0.036 | 2.41 | 2100 | 2.50 | 0.16 | | CI |
| 12 | | 57 | 5 | 1 | 41.0 | 1.5 | 0.036 | 2.41 | 1500 | 2.50 | 0.24 | | CI |
| 13 | | 88 | 4 | 1 | 41.0 | 11.0 | 0.052 | 3.85 | 11 000 | 4.06 | 0.02 | | KH |
| 14 | C1 | 88 | 4 | 1 | 41.0 | 7.0 | 0.052 | 3.85 | 7000 | 4.06 | 0.04 | I, II | KH |
| 15 | C2 | 88 | 4 | 1 | 41.0 | 4.6 | 0.052 | 3.85 | 4600 | 4.06 | 0.06 | I, II | KH |
| 16 | C3 | 88 | 4 | 1 | 41.0 | 3.0 | 0.052 | 3.85 | 3000 | 4.06 | 0.10 | I, II | KH |
| 17 | | 88 | 4 | 1 | 41.0 | 2.1 | 0.052 | 3.85 | 2100 | 4.06 | 0.16 | | CI |
| 18 | | 88 | 4 | 1 | 41.0 | 1.5 | 0.052 | 3.85 | 1500 | 4.06 | 0.24 | | CI |
| 19 | | 132 | 3.4 | 1 | 43.5 | 11.0 | 0.070 | 6.03 | 11 000 | 6.49 | 0.02 | | SS |
| 20 | D1 | 132 | 3.4 | 1 | 43.5 | 7.0 | 0.070 | 6.03 | 7000 | 6.49 | 0.04 | II, III | KH |
| 21 | D2 | 132 | 3.4 | 1 | 43.5 | 4.6 | 0.070 | 6.03 | 4600 | 6.49 | 0.06 | I, II, III | KH |
| 22 | | 132 | 3.4 | 1 | 43.5 | 3.0 | 0.070 | 6.03 | 3000 | 6.49 | 0.11 | | KH |
| 23 | D3 | 132 | 3.4 | 1 | 43.5 | 2.1 | 0.070 | 6.03 | 2100 | 6.49 | 0.17 | I, II, III | CI |
| 24 | | 132 | 3.4 | 1 | 43.5 | 1.5 | 0.070 | 6.03 | 1500 | 6.49 | 0.26 | | CI |
| 25 | | 132 | 3.4 | 1 | 43.5 | 1.0 | 0.070 | 6.03 | 1000 | 6.49 | 0.43 | | CI |
| 27 | | 180 | 3 | 1 | 43.0 | 11.0 | 0.097 | 9.59 | 11 000 | 10.62 | 0.02 | | SS |
| 28 | E1 | 180 | 3 | 1 | 43.0 | 7.0 | 0.097 | 9.59 | 7000 | 10.62 | 0.04 | II | SS |
| 29 | | 180 | 3 | 1 | 43.0 | 4.6 | 0.097 | 9.59 | 4600 | 10.62 | 0.06 | | SS |
| 30 | | 180 | 3 | 1 | 43.0 | 3.0 | 0.097 | 9.59 | 3000 | 10.62 | 0.11 | | KH |
| 31 | | 180 | 3 | 1 | 43.0 | 2.1 | 0.097 | 9.59 | 2100 | 10.62 | 0.17 | | KH |
| 32 | | 180 | 3 | 1 | 43.0 | 1.5 | 0.097 | 9.59 | 1500 | 10.62 | 0.26 | | CI |
| 33 | | 180 | 3 | 1 | 43.0 | 1.0 | 0.097 | 9.59 | 1000 | 10.62 | 0.43 | | CI |
| 34 | | 221 | 2.5 | 1 | 41.0 | 11.0 | 0.131 | 17.44 | 11 000 | 20.08 | 0.02 | | SS |

Table 3. For caption see on next page.

| Case | Name | N | G/d | d (cm) | D (cm) | h (cm) | ϕ | aD | Re _h | Γ_D | S _C | Velocity measurement type | Wake regime |
|------|------|-----|-----|--------|--------|--------|--------|----------|-----------------|------------|----------------|---------------------------|-------------|
| 35 | F1 | 221 | 2.5 | 1 | 41.0 | 7.0 | 0.131 | 17.44 | 7000 | 20.08 | 0.04 | I, II, IV | SS |
| 36 | | 221 | 2.5 | 1 | 41.0 | 4.6 | 0.131 | 17.44 | 4600 | 20.08 | 0.06 | | SS |
| 37 | F2 | 221 | 2.5 | 1 | 41.0 | 3.0 | 0.131 | 17.44 | 3000 | 20.08 | 0.10 | | SS |
| 38 | | 221 | 2.5 | 1 | 41.0 | 2.1 | 0.131 | 17.44 | 2100 | 20.08 | 0.16 | | KH |
| 39 | | 221 | 2.5 | 1 | 41.0 | 1.5 | 0.131 | 17.44 | 1500 | 20.08 | 0.24 | | CI |
| 40 | | 221 | 2.5 | 1 | 41.0 | 1.0 | 0.131 | 17.44 | 1000 | 20.08 | 0.41 | | CI |
| 41 | | 339 | 2 | 1 | 41.0 | 11.0 | 0.202 | 35.16 | 11 000 | 44.05 | 0.02 | | SS |
| 42 | | 339 | 2 | 1 | 41.0 | 7.0 | 0.202 | 35.16 | 7000 | 44.05 | 0.04 | | SS |
| 43 | | 339 | 2 | 1 | 41.0 | 4.6 | 0.202 | 35.16 | 4600 | 44.05 | 0.06 | | SS |
| 44 | | 339 | 2 | 1 | 41.0 | 3.0 | 0.202 | 35.16 | 3000 | 44.05 | 0.10 | | SS |
| 45 | | 339 | 2 | 1 | 41.0 | 2.1 | 0.202 | 35.16 | 2100 | 44.05 | 0.16 | | SS |
| 46 | | 339 | 2 | 1 | 41.0 | 1.5 | 0.202 | 35.16 | 1500 | 44.05 | 0.24 | | KH |
| 47 | | 339 | 2 | 1 | 41.0 | 1.0 | 0.202 | 35.16 | 1000 | 44.05 | 0.41 | | CI |
| 48 | | 502 | 1.7 | 1 | 43.5 | 11.0 | 0.265 | 62.36 | 11 000 | 84.87 | 0.02 | I, II | SS |
| 49 | G1 | 502 | 1.7 | 1 | 43.5 | 7.0 | 0.265 | 62.36 | 7000 | 84.87 | 0.04 | | SS |
| 50 | | 502 | 1.7 | 1 | 43.5 | 4.6 | 0.265 | 62.36 | 4600 | 84.87 | 0.06 | | SS |
| 51 | G2 | 502 | 1.7 | 1 | 43.5 | 3.0 | 0.265 | 62.36 | 3000 | 84.87 | 0.11 | II | SS |
| 52 | | 502 | 1.7 | 1 | 43.5 | 2.1 | 0.265 | 62.36 | 2100 | 84.87 | 0.17 | | SS |
| 53 | | 502 | 1.7 | 1 | 43.5 | 1.5 | 0.265 | 62.36 | 1500 | 84.87 | 0.26 | | KH |
| 54 | | 502 | 1.7 | 1 | 43.5 | 1.0 | 0.265 | 62.36 | 1000 | 84.87 | 0.43 | | KH |
| 55 | | 651 | 1.5 | 1 | 43.0 | 11.0 | 0.352 | 103.03 | 11 000 | 159.01 | 0.02 | | SS |
| 56 | | 651 | 1.5 | 1 | 43.0 | 7.0 | 0.352 | 103.03 | 7000 | 159.01 | 0.04 | | SS |
| 57 | | 651 | 1.5 | 1 | 43.0 | 4.6 | 0.352 | 103.03 | 4600 | 159.01 | 0.06 | | SS |
| 58 | | 651 | 1.5 | 1 | 43.0 | 3.0 | 0.352 | 103.03 | 3000 | 159.01 | 0.11 | | SS |
| 59 | | 651 | 1.5 | 1 | 43.0 | 2.1 | 0.352 | 103.03 | 2100 | 159.01 | 0.17 | | SS |
| 60 | | 651 | 1.5 | 1 | 43.0 | 1.5 | 0.352 | 103.03 | 1500 | 159.01 | 0.26 | | SS |
| 61 | | 788 | 1.3 | 1 | 41.3 | 11.0 | 0.462 | 165.99 | 11 000 | 308.53 | 0.02 | I, II | VS |
| 62 | H1 | 788 | 1.3 | 1 | 41.3 | 7.0 | 0.462 | 165.99 | 7000 | 308.53 | 0.04 | | VS |
| 63 | | 788 | 1.3 | 1 | 41.3 | 4.6 | 0.462 | 165.99 | 4600 | 308.53 | 0.06 | | VS |
| 64 | | 788 | 1.3 | 1 | 41.3 | 3.0 | 0.462 | 165.99 | 3000 | 308.53 | 0.10 | | VS |
| 65 | | 788 | 1.3 | 1 | 41.3 | 2.1 | 0.462 | 165.99 | 2100 | 308.53 | 0.16 | | SS |
| 66 | | 788 | 1.3 | 1 | 41.3 | 1.5 | 0.462 | 165.99 | 1500 | 308.53 | 0.25 | | SS |
| 67 | H2 | 788 | 1.3 | 1 | 41.3 | 1.0 | 0.462 | 165.99 | 1000 | 308.53 | 0.41 | II, III | KH |
| 68 | J | 1 | 0 | — | 41.3 | 7.0 | 1 | ∞ | 7000 | ∞ | 0.04 | I, II | VS |

Table 3. For caption see on next page.

| Case | Name | N | G/d | d (cm) | D (cm) | h (cm) | ϕ | aD | Re_h | Γ_D | S_C | Velocity measurement type | Wake regime |
|------|------|-----|-------|----------|----------|----------|--------|----------|--------|------------|-------|---------------------------|-------------|
| 69 | | 1 | 0 | — | 41.3 | 4.6 | 1 | ∞ | 4600 | ∞ | 0.06 | | VS |
| 70 | | 1 | 0 | — | 41.3 | 3.0 | 1 | ∞ | 3000 | ∞ | 0.10 | | VS |
| 71 | | 1 | 0 | — | 41.3 | 2.1 | 1 | ∞ | 2100 | ∞ | 0.16 | | VS |
| 72 | A1* | 19 | 5 | 1 | 23.3 | 4.3 | 0.034 | 1.30 | 3300 | 1.34 | 0.04 | V | CI |
| 73 | B1* | 18 | 3.4 | 1 | 16.2 | 3.3 | 0.069 | 2.14 | 3300 | 2.30 | 0.04 | V | KH |
| 74 | C3* | 35 | 3 | 1 | 20.0 | 1.7 | 0.085 | 3.73 | 2100 | 4.09 | 0.10 | V | KH |
| 75 | D2* | 33 | 2.5 | 1 | 16.0 | 2.1 | 0.129 | 5.27 | 2100 | 6.06 | 0.06 | V | KH |
| 76 | E1* | 41 | 2 | 1 | 15.5 | 3.1 | 0.171 | 8.98 | 3300 | 10.80 | 0.04 | V | SS |
| 77 | F2* | 103 | 2 | 1 | 23.6 | 2.0 | 0.185 | 16.38 | 2000 | 20.10 | 0.10 | | SS |
| 78 | D3* | 69 | 2.5 | 1 | 24.0 | 3.0 | 0.120 | 3.66 | 2400 | 8.12 | 0.06 | III | KH |
| 79 | | — | — | — | — | 1.5 | — | — | — | — | — | | — |
| 80 | | — | — | — | — | 2.1 | — | — | — | — | — | | — |
| 81 | | — | — | — | — | 3.0 | — | — | — | — | — | | — |
| 82 | | — | — | — | — | 4.6 | — | — | — | — | — | | — |
| 83 | | — | — | — | — | 7.0 | — | — | — | — | — | | — |

Table 3. Experimental conditions employed in this study. Testing cases numbered from '79' to '83' represent the dye visualisation cases without array models. Cases with numbered text (e.g. 'A1') are those for which wake velocity fields were measured and roman numeral (e.g. 'I') denotes the type of velocity measurement.

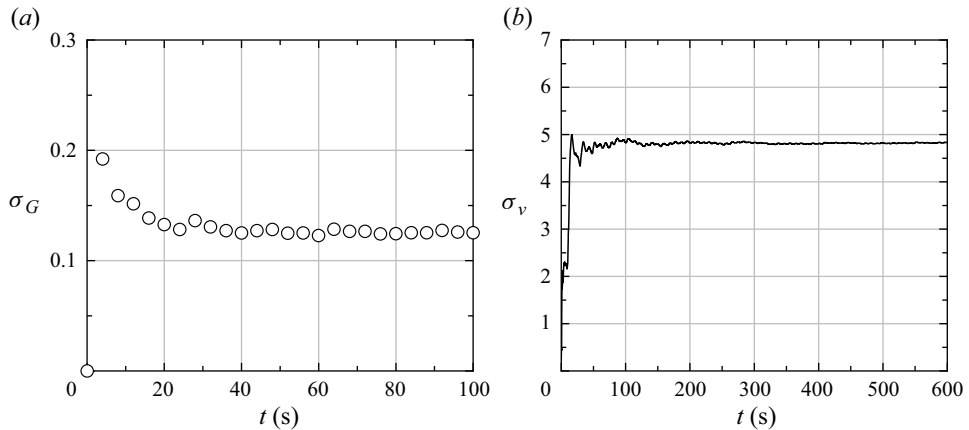


Figure 2. Variations of temporal standard deviation of (a) green colour intensity (σ_G) and (b) transverse velocity (σ_v) with sample length (t) in case H1 (table 3). The horizontal axis t represents the width of a time window (starting from zero) over which σ_G and σ_v were calculated. The convergence of σ_G at a time of 45 seconds and of σ_v at a time of 260 seconds suggests that sampling periods of 100 and 300 seconds for data from the flow visualisation and velocity measurements, respectively, met statistical convergence.

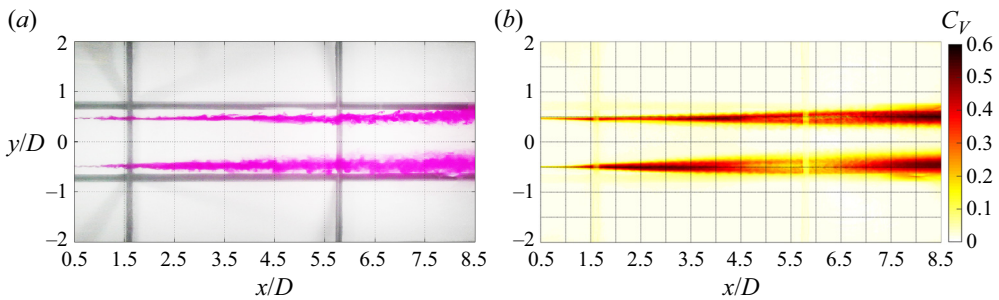


Figure 3. Evolution of dye streaks in the flow ($h = 7$ cm) with no array. (a) Instantaneous streak structure; (b) the spatial distribution of C_V . The array diameter D used for normalisation is equal to 43 cm. There is lateral spreading of dye streaks due to ‘background’ diffusion, which will be used as a point of comparison for dye streaks in the presence of cylinder arrays.

velocity (White & Nepf 2007). At each measurement location, the velocity was sampled for 5 mins at a frequency of 25 Hz. As an example, the standard deviation of $v(t)$ (σ_v) sampled at $(x/D, y/D) = (3, 0)$ was converged at a length of 260 seconds after which $(\sigma_{v,t} - \sigma_{v,t+\Delta t})/\Delta t < 2\%$ for case H1 (see figure 2b), suggesting the velocity sample duration (300 s) was statistically sufficient. Measurement durations of 600 and 1200 s were required in certain cases to examine the strongly oscillating near wake flow ($x/D = 1$) of regime VS and the intermittent velocity oscillations of regime KH (introduced later), respectively. Each velocity record was decomposed into time-averaged (\bar{u}, \bar{v}) and fluctuating components (u', v'). The turbulence intensity in the ambient flow was calculated as $\sqrt{u'^2}/U_\infty$, which was typically less than 3%. Spectra of transverse velocity were used to examine oscillations in the wake; all spectra were smoothed using a Parzen window of width 10. The continuous wavelet transform in MATLAB was used to obtain the spectrogram of $v'(t)$, to examine the variation of oscillation frequency with time.

2.3. Test matrix

The testing conditions for all cases are detailed in [table 3](#). In total, flow visualisation was performed across 78 experimental cases to assess the variation of wake structure across the parameter space. Among these, detailed velocity measurements were undertaken in 22 cases ([table 3](#)) to achieve the following five objectives:

- (I) to investigate the evolution of array shear layers, five transverse profiles were measured along $x/D = 1.0, 3.0, 5.0, 7.0$ and 8.5 , respectively, for 14 cases. Each transverse profile was sampled from $y/D = 0$ to 1.6 , which included 20 data locations, on average;
- (II) to quantify the bleeding flow, velocities at $(x/D, y/D) \approx 0.5$ were measured;
- (III) to confirm the wake classification by flow visualisation, point measurements at $(x/D, y/D) = (7, 0.5), (8.5, 0.5)$ and $(8.5, 0)$ were collected in some cases near the regime transition boundaries;
- (IV) to quantify the length of the steady wake region, velocities along the line of $y/D = 0.05$ were measured from $x/D = 0.5$ to 8.5 with high resolution in case F1;
- (V) to confirm that the array-scale wake structure is independent of array size, the wake profiles for the small arrays were measured at $x/D = 1.0$ for comparison to those of large arrays.

The sample locations for I, II and IV are sketched in [figure 1\(a\)](#) as typical examples for the transverse profile, streamwise profile and point measurement, respectively. Each type of velocity measurement is denoted by I, II, III, IV, V in [table 3](#), respectively.

3. Results

3.1. Wake regimes in shallow flow through an array of cylinders

3.1.1. Wake classification

By varying flow blockage and wake stability parameters, four wake regimes are observed behind an array of cylinders in the present experimental program: (i) vortex street wake (VS); (ii) ‘steady + shedding’ wake (SS); (iii) Kelvin–Helmholtz instability wake (KH); and (iv) coupled individual wake (CI).

[Figure 4](#) illustrates the key flow characteristics in each wake regime. The first column shows a snapshot of dye streaks to visualise the instantaneous wake structure (see also the supplementary movies 1–5 available at <https://doi.org/10.1017/jfm.2024.338>), the second column presents C_V to indicate the time-averaged wake structure and the third column plots the power spectral density of the transverse velocity at $(x/D, y/D) = (8.5, 0.5)$.

Regime VS is characterised by a classical von Kármán vortex street formed immediately behind the array ([figure 4a](#)). The time-averaged wake structure behind the cylinder array ([figure 4b](#)) is similar to the classical wake of a single solid cylinder (Zdravkovich 1997). At any given streamwise location, the value of C_V is higher near the wake boundaries than along the wake centreline. Near the wake boundaries, von Kármán vortices continuously entrain the ambient uncoloured fluid into the wake, leading to a sharp change in temporal variation of colour intensity C_V from nearly zero to very high values. The von Kármán vortex street behind the cylinder array creates a sharp peak in the spectrum of transverse velocity ([figure 4c](#)). The corresponding array Strouhal number (defined as $St_D = fD/U_\infty$) for the case shown is 0.23, which is close to the value ($St_D \approx 0.2$) of an isolated solid cylinder in a vertically unbounded flow (Sumer & Fredsøe 1997). Cylinder arrays in the VS regime thus behave similarly to a single solid obstacle in terms of the wake structure.

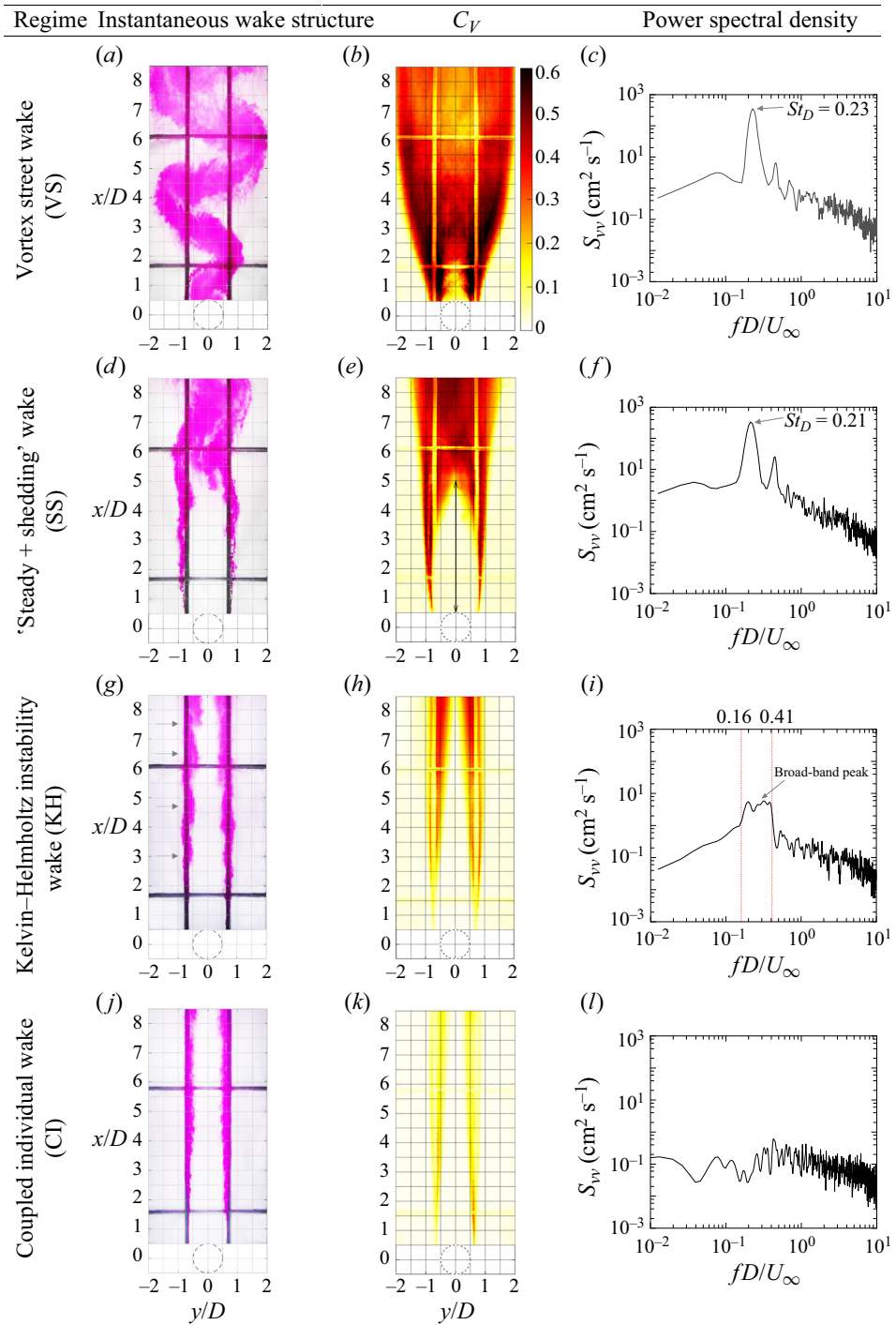


Figure 4. Wake regimes are well distinguished by the instantaneous wake structure (snapshot of dye streaks), the time-averaged flow structure (field of C_V) and power spectral density (S_{vv}) of transverse velocity. The incoming flow is directed upwards. Transverse velocities v for calculating the spectra were sampled at $(x/D, y/D) = (8.5, 0.5)$. The four rows present (in order) cases H1, F1, C1 and A1. The steady wake region in panel (e) is roughly indicated by the black arrow. The series of KH vortices formed in the array shear layer in regime KH in panel (g) is marked by grey arrows.

The ‘steady + shedding’ wake (SS) is characterised by a steady wake region attached behind the array, followed downstream by a von Kármán vortex street. The two array shear layers remain stable in the steady region, before interacting to result in the vortex street downstream. The merging of the dye streaks at the wake centreline (at $x/D \approx 5$ in [figure 4d](#)) coincides with the end of the steady wake region, as demonstrated by Zong & Nepf (2012). The steady wake region is delineated approximately by a region of nearly zero C_V in [figure 4\(e\)](#). The vortex street is associated with a sharp peak in the spectrum at $St_D = 0.21$ ([figure 4f](#)), which is again similar to that of a single solid cylinder. The formation of a steady wake region immediately downstream of the array is the key feature that differentiates regime SS from regime VS.

The regime KH is identified by the occurrence of a Kelvin–Helmholtz (KH) instability in the array shear layers, through flow visualisation and analysis of the velocity spectrum (described in more detail in § 3.1.3). The array-scale KH vortices (grey arrows in [figure 4g](#)) are distinctly different from those in regimes SS and VS in four ways:

- (i) the two dye streaks do not mix together at the location where the vortices are initially formed, suggesting the vortices are not generated through the direct interaction between the two shear layers, i.e. vortex shedding;
- (ii) the rows of coherent vortices within each array shear layer are not shed from alternating sides of the array (see also the online supplementary movie 3), which indicates that there is minimal temporal correlation between the coherent structures across the two shear layers. This is distinct from that observed in the SS regime where the von Kármán vortices are shed alternately from either side of the array (supplementary movie 2);
- (iii) at a given streamwise location, the KH vortices are barely perceptible within either array shear layer at some instants, whereas at other instants, discrete KH vortices had developed in the shear layer (see supplementary movies 3 and 4). This indicates the irregular generation of coherent vortices in array shear layers;
- (iv) the frequency content of the wake is different. In contrast to the narrow-banded peak in regimes SS and VS ([figure 4c,f](#)), a broadband peak is detected within the array shear layers in the KH regime ([figure 4i](#)). The broadband peak, defined as the range in which the power spectral density is larger than 20% of its maximum, is in the range of approximately $0.16 < fD/U_\infty < 0.41$. The broadband peak is indicative of a KH instability in shear flows with a convective nature (Cardell 1993; Prasad & Williamson 1997; White & Nepf 2007).

In the coupled individual wake (CI), the wakes from the elements of the array are the dominant flow feature in the array wake. The array shear layers still exist in this regime, but they are stable, such that no KH instability or vortex shedding occurs. This is indicated by the similarity of downstream evolution of dye streaks to that of the case without the array (see [figures 3a](#) and [4j](#)). The dye streaks expand in the transverse direction smoothly downstream, without rolling up into any coherent vortex structures ([figure 4j](#)). The C_V value is high near the array and decreases along the wake for regime CI ([figure 4k](#)), which is indicative of lower lateral mixing rate downstream and hence no instability developing in the array shear layers in regime CI. The stabilisation of the wake flow is also confirmed by the velocity spectrum, with no identifiable dominant frequency across the entire frequency range ([figure 4l](#)).

The differences in the dye streak pattern, spatial C_V distribution and spectrum between these four regimes demonstrate the generation of stable array shear layers in regime CI and unstable array shear layers creating coherent vortex structures in regimes KH, SS and VS.

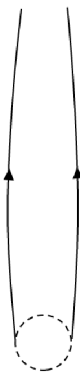

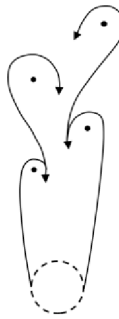

| Regime | Coupled individual wake (CI) | KH instability wake (KH) | 'Steady + shedding' wake (SS) | Vortex street wake (VS) |
|--|---|---|--|--|
| Principal feature | Array shear layers are stable and the array wake is dominated by wakes of individual elements | Array shear layers are susceptible to Kelvin–Helmholtz instability, without resulting in von Kármán vortex shedding | A steady wake region immediately downstream of the array is followed by a von Kármán vortex street | A von Kármán vortex street is formed immediately behind the array |
| Array shear layer | Stable | Unstable | Unstable | Unstable |
| Steady wake region | Yes | Yes | Yes | No |
| Von Kármán vortex shedding (in the array wake) | No | No | Yes | Yes |
| Schematic of wake structure |  |  |  |  |

Table 4. Characteristic flow features of the four wake regimes behind an array of cylinders. Dashed circle represents the edge of a cylinder array, and the incident flow points upwards. Shear layers are considered 'unstable' when they generate coherent vortex structures.

A summary of principal features for these four regimes is given in [table 4](#), together with a schematic of the wake structure for each regime.

3.1.2. Controlling influence of Γ_D and S_C on wake structure

The wake flow regimes observed behind 71 large arrays of cylinders ($D/d \approx 42.5$) in shallow flow are mapped out in the (Γ_D, S_C) parameter space in [figure 5](#) (solid symbols), combined with existing data (hollow symbols). From the bottom-right corner to the top-left corner of the Γ_D – S_C plane, the wake structure varies from a vortex street wake (VS) to a 'steady + shedding' wake (SS), then to a Kelvin–Helmholtz instability wake (KH), and finally to a 'coupled individual wake' (CI). This indicates that increases in S_C and reductions in Γ_D tend to suppress the generation of large-scale coherent vortex structures, resulting in more stable wakes.

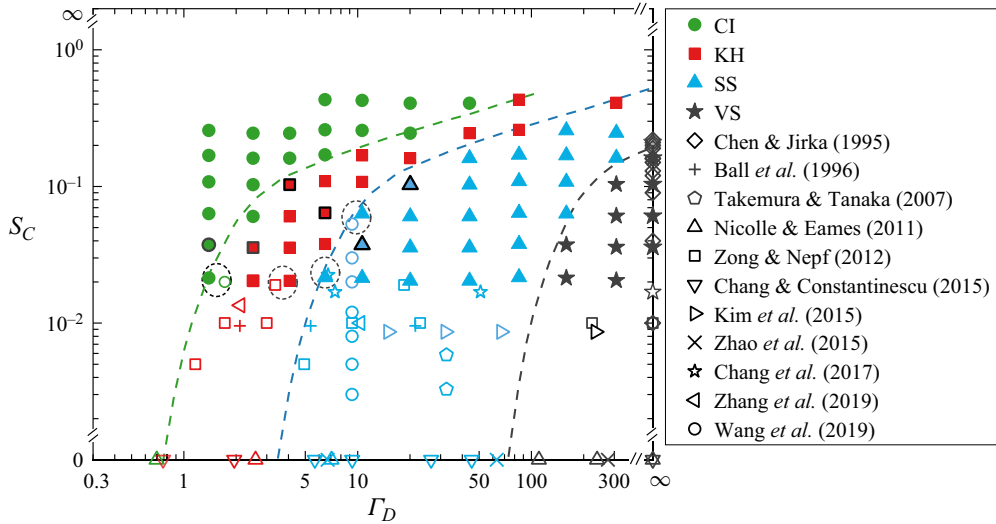


Figure 5. Separation, in the S_C – Γ_D parameter space, of wake regimes in flows through an array of cylinders. Filled and unfilled markers represent data from this work and previous studies, respectively. Six filled symbols with black edges represent the pairs of cases tested with arrays of both large and small dimensionless array sizes (D/d). The dashed ellipses denote two cases with close values of Γ_D or S_C , but with an approximately 50% difference in D/d . This chart shows that a wake transition can be caused by variation of either Γ_D or S_C and allows prediction of the wake regime behind an array of cylinders.

Figure 5 shows that data points generated with these large arrays and compiled from the literature, associated with each regime, cluster together within the parameter space. Data points of each regime are separated, forming clear boundary lines between them (as delineated by dashed lines). This clear separation suggests that the wake structure is, to first order, controlled by flow blockage and wake stability parameters, as hypothesised in § 1.

The curved regime boundaries between regimes implies that the wake structure behind a cylinder array depends on both Γ_D and S_C nonlinearly. With increasing S_C , the regime boundary lines become increasingly horizontal (figure 5). This indicates that wake transition depends increasingly on S_C as it increases. Figure 5 suggests that there is an upper limited for $S_C \approx 0.6$ above which only regime CI is found. This is expected as for $S_C \gtrsim 0.6$ the wake flow is fully stabilised without any oscillation for an isolated cylinder (Chen & Jirka 1997). The isolated cylinder, however, has much stronger shear layers than the cylinder array (demonstrated later in § 4.2) and, unlike the porous array, there is no stabilising influence of bleeding flow on the wake. This suggests that $S_C \approx 0.6$ is conservative for the cylinder array, above which all the instability associated with array shear layers will be completely suppressed. Increasing Γ_D can have a similar effect to decreasing S_C in causing transitions between regimes. Because of the nonlinear dependency, it is difficult to collapse Γ_D and S_C down to one single parameter that defines the wake structure.

As bleeding flow has controlling influence on the wake structure (Wood 1967; Zong & Nepf 2012; Chang & Constantinescu 2015), especially at low wake stability parameter, the shape of the boundary lines between different regimes can be interpreted by scaling terms in the momentum equation. Within the array, the time-mean flow in the streamwise

direction is governed by the following equation:

$$\bar{u} \frac{\partial \bar{u}}{\partial x} + \bar{v} \frac{\partial \bar{u}}{\partial y} = -\frac{1}{\rho} \frac{\partial \bar{p}}{\partial x} - \frac{C_{da}}{2(1-\phi)} \bar{u}(\bar{u}^2 + \bar{v}^2)^{1/2} - \frac{C_f}{2h} \bar{u}(\bar{u}^2 + \bar{v}^2)^{1/2}, \quad (3.1)$$

where \bar{p} is the time-mean pressure. Similarly, the diverted flow in the streamwise direction at either side of the array is controlled by

$$\bar{u} \frac{\partial \bar{u}}{\partial x} + \bar{v} \frac{\partial \bar{u}}{\partial y} = -\frac{1}{\rho} \frac{\partial \bar{p}}{\partial x} - \frac{C_f}{2h} \bar{u}(\bar{u}^2 + \bar{v}^2)^{1/2}. \quad (3.2)$$

When the array flow blockage (Γ_D) is low, it is normally assumed that the pressure gradient ($\partial \bar{p} / \partial x$) approaches zero and hence the pressure terms in both (3.1) and (3.2) drop out; if the array flow blockage is high, the flow will become fully developed with the streamwise pressure gradient in the array equal to that in the diverted flow, and hence the pressure gradients in (3.1) and (3.2) are cancelled out (Rominger & Nepf 2011). To first approximation, the fraction of flow passing through the array (bleeding flow velocity, \bar{u}_b) therefore depends on the ratio between the flow resistances in the array and in the diverted flow as

$$\frac{\bar{u}_b}{U_\infty} = f \left(\frac{-\frac{C_f}{2h} \bar{u}(\bar{u}^2 + \bar{v}^2)^{1/2}}{-\frac{C_{da}}{2(1-\phi)} \bar{u}(\bar{u}^2 + \bar{v}^2)^{1/2} - \frac{C_f}{2h} \bar{u}(\bar{u}^2 + \bar{v}^2)^{1/2}} \right). \quad (3.3)$$

Simplifying (3.3) gives

$$f^{-1} \left(\frac{\bar{u}_b}{U_\infty} \right) = \frac{S_C}{S_C + \Gamma_D}. \quad (3.4)$$

Rearranging (3.4) yields

$$S_C = \frac{f^{-1} \left(\frac{\bar{u}_b}{U_\infty} \right)}{1 - f^{-1} \left(\frac{\bar{u}_b}{U_\infty} \right)} \Gamma_D. \quad (3.5)$$

With a critical value of $f^{-1}(\bar{u}_b/U_\infty)$, the relationship in (3.5) for the bleeding flow can be mapped out into the S_C - Γ_D space, which sets a boundary line between the two adjacent regimes in the regime chart in figure 5. Clearly, for a constant value of $f^{-1}(\bar{u}_b/U_\infty)$, S_C is proportional to Γ_D and hence the boundary line between each of the two adjacent regimes (e.g. CI, KH) should be a straight line in the log-scale regime chart. This is valid only when the wake stability parameter is low and the influence of bleeding flow dominates the wake transition. For a high value of S_C , the bed friction not only affects the bleeding flow velocity (as described in (3.5)) but also plays an important role in suppressing the instabilities in the far wake. This suppression effect of bed friction on the instabilities has been demonstrated for the single mixing layer (Chu *et al.* 1991) and the wake behind an isolated cylinder (Chen & Jirka 1995, 1997) in shallow water. This suppression effect will be demonstrated for an array of cylinders later in § 4.1.2. With this bed friction effect on wake instabilities, the boundary lines between adjacent regimes should deviate downwards from linear lines for a high value of S_C .

These scaling arguments are consistent with the experimental observations. Figure 5 shows that the boundary lines between different regimes are close to linear at $S_C \lesssim 0.1$, whereas boundary lines increasingly deviate downwards from linear lines to be horizontal

| Case | ϕ | D/d | h (cm) | Γ_D | S_C | Wake regime |
|------|--------|-------|----------|------------|-------|-------------|
| A1 | 0.022 | 43.0 | 7.0 | 1.39 | 0.04 | CI |
| A1* | 0.034 | 23.3 | 4.3 | 1.34 | 0.04 | CI |
| B1 | 0.036 | 41.0 | 7.0 | 2.50 | 0.04 | KH |
| B1* | 0.069 | 16.2 | 3.3 | 2.33 | 0.04 | KH |
| C3 | 0.052 | 41.0 | 3.0 | 4.07 | 0.10 | KH |
| C3* | 0.085 | 20.0 | 1.7 | 4.10 | 0.10 | KH |
| D2 | 0.070 | 43.5 | 4.6 | 6.48 | 0.06 | KH |
| D2* | 0.129 | 16.0 | 2.1 | 6.05 | 0.06 | KH |
| E1 | 0.097 | 43.0 | 7.0 | 10.62 | 0.04 | SS |
| E1* | 0.171 | 15.5 | 3.1 | 10.83 | 0.04 | SS |
| F2 | 0.131 | 41.0 | 3.0 | 20.09 | 0.10 | SS |
| F2* | 0.185 | 23.6 | 2.0 | 20.10 | 0.10 | SS |

Table 5. Comparison of visualised wake regimes for pairs of cases with the same values of Γ_D and S_C , but different size (D/d). Note that the cylinder diameters for all cases are $d = 1$ cm. In all pairs, there is no change of wake form when the array diameter is halved, confirming that the wake structure is primarily controlled by Γ_D and S_C .

with the increase of S_C for $S_C \gtrsim 0.1$. This indicates that the wake transitions for $S_C \lesssim 0.1$ and $S_C \gtrsim 0.1$ are primarily governed by the array-induced flow blockage and shallowness, respectively.

The regime chart in figure 5 is initially established by varying the water depth while keeping the array diameter virtually constant ($D \approx 42.5$ cm) since it is more effective to change S_C through varying h rather than D . This means that the observed wake transition along the S_C -axis of the regime chart reflects the influence of limited water depth rather than the complete range of S_C . To further demonstrate the controlling influence of S_C and Γ_D , here, the dependence of this regime chart on the array size D/d is explored. In particular, the model array diameter was halved in the particular cases that fell near regime boundaries (symbols with black edge in figure 5), while maintaining the same values of S_C , Γ_D and d (cases ‘72–77’ listed in table 3).

Flow visualisation shows that halving the array diameter has minimal impact on the wake structure. In total, six pairs of scenarios in the neighbourhood of regime boundaries were examined (see table 5). It is seen that flows with the same governing parameter set (Γ_D , S_C) but with an approximately 50% difference in D/d display the same wake form. This independence of wake structure on the dimensionless array size is also confirmed through measurement of the transverse profile of mean velocity in the wake. There is good agreement of transverse profiles of streamwise velocity (\bar{u}/U_∞) at $x/D = 1$ between the large and small arrays with the same values of Γ_D and S_C (see figure 6).

The independence of this regime chart on dimensionless array size is also confirmed by the consistency of wake regimes between different studies for the same values of Γ_D and S_C . Table 6 summarises the broad range of dimensionless array size (D/d), Reynolds numbers defined based on the element diameter (Re_d), array diameter (Re_D) and water depth (Re_h) for independent studies. Despite large difference in values of D/d , Re_d , Re_D and Re_h , near the transition boundaries, the data points with close values of Γ_D , S_C lie in the same wake regimes (CI, KH, SS). For instance, the data points from the present study and those from existing work (Zong & Nepf 2012; Chang *et al.* 2017; Wang *et al.* 2019) (marked with dashed ellipses in figure 5) with close values of Γ_D and S_C all share the same wake regimes despite their D/d values varying by a factor of two. In summary, the similarity of wake structures between arrays with the same values of Γ_D and S_C

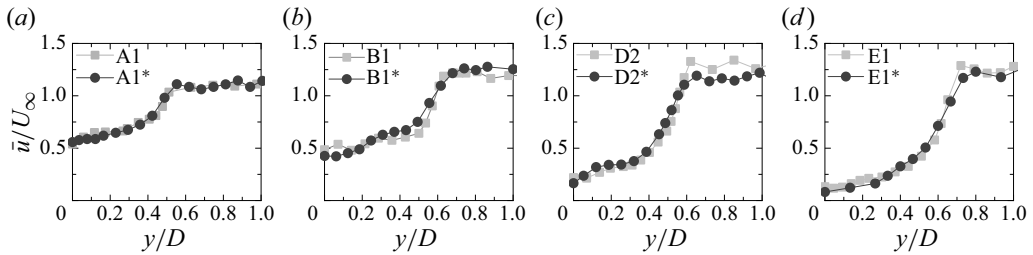


Figure 6. Comparison of wake profiles of \bar{u}/U_∞ at $x/D = 1$ between the cases of large and small D/d values. The pair of cases in each panel have the same values of Γ_D and S_C , but an approximately 50% difference in D/d . There is negligible difference between the pair of velocity profiles in panels (a)–(d), demonstrating the independence of wake structure on the array size.

but different values of D/d (in the range $3.5 < D/d < 81.9$) demonstrates the controlling influence of flow blockage and wake stability parameters on wake structure, and thus the insensitivity of this regime chart to array size.

Provided that one knows the array geometry, and the depth and velocity of the incident flow (allows for calculation of Γ_D and S_C), this regime chart can be used to predict wake structure behind a cylinder array across entire relevant practical parameter space.

3.1.3. Regime KH

Regimes VS, SS and CI in vertically unbounded flow are well established in the literature and demonstrated for the shallow flow in § 3.1.1. In comparison to this, the identification of the new regime KH is more novel and needs to be further established.

To start it is useful to demonstrate the consistency between the observed peak frequencies in the spectrum of transverse velocity and those predicted from linear stability analysis of a classical mixing layer (e.g. Ho & Huerre 1984). The analogy between an array shear layer and a mixing layer serves as the basis for this demonstration. The velocity profile in a mixing layer can be described by a hyperbolic tangent function:

$$\frac{\bar{u} - \bar{U}}{\Delta U} = \frac{1}{2} \tanh \frac{y - \bar{y}}{2\theta}, \quad (3.6)$$

where \bar{U} is the arithmetic mean of \bar{u}_1 and \bar{u}_2 (low- and high-stream velocities), $\Delta U = \bar{u}_2 - \bar{u}_1$, \bar{y} is the transverse location where $\bar{u} = \bar{U}$, and θ is the momentum thickness of the mixing layer, defined as

$$\theta = \int_{-\infty}^{\infty} \left[\frac{1}{4} - \left(\frac{\bar{u} - \bar{U}}{\Delta U} \right)^2 \right] dy. \quad (3.7)$$

Velocity profiles in array shear layers within regime KH collapse to this hyperbolic tangent function (figure 7). As the shear layer profile remains self-similar, this collapse is independent of downstream location. The consistency between the experimental and analytical results indicates that the array shear layers are analogous to classical mixing layers.

In the linear local stability analysis, infinitesimal perturbations of the stream function can be defined in the form:

$$\psi(x, y, t) = \eta(y) e^{-i(\alpha x - \omega t)} + \text{c.c.}, \quad (3.8)$$

where $\omega = 2\pi f$ is the angular frequency, α is the wave number, c.c. represents the complex conjugate, and the eigenfunction of $\eta(y)$ can be obtained by solving the linear Rayleigh

| Data sources | D/d | Re_d | Re_D | Re_h | Symbol in figure 5 |
|-------------------------------|-----------------------|------------------|----------------|----------------|--------------------|
| Present study | 15.5–43.5 | 1000 | 1550–43 500 | 1000–11 000 | Filled |
| Chen & Jirka (1995) | 1 (isolated cylinder) | 3000–414 000 | 3000–414 000 | 570–7300 | ◇ |
| Ball <i>et al.</i> (1996) | 21.1–81.9 | 900–3500 | 820 000 | 35 000 | + |
| Takemura & Tanaka (2007) | 3.5–4.0 | 1000 | 14 000–16 000 | 20 000 | ◊ |
| Nicolle & Eames (2011) | 21.0 | 100 | 2100 | — | △ |
| Zong & Nepf (2012) | 16.7–70.0 | 588 | 9800–41 160 | 13 034 | □ |
| Chang & Constantinescu (2015) | 10.4–20.8 | 480–960 | 10 000 | — | ▽ |
| Kim <i>et al.</i> (2015) | 36.7 | 588 | 21 560 | — | ▷ |
| Zhao <i>et al.</i> (2015) | 8.5–26.0 | 100 | 850–26 000 | — | × |
| Chang <i>et al.</i> (2017) | 16.7, 36.7 | 1125, 2010, 4020 | 37 500, 76 000 | 15 000, 20 100 | ☆ |
| Zhang <i>et al.</i> (2019) | 36.7 | 680 | 24 936 | — | ◁ |
| Wang <i>et al.</i> (2019) | 36.7 | 588 | 21 562 | 6517–26 068 | ○ |

Table 6. Summary of array size (D/d), Reynolds number defined based on element diameter (Re_d), array diameter (Re_D) and water depth (Re_h) for different studies shown in figure 5. Note that the velocity upstream of the obstacle is used in the definitions of different Reynolds numbers. Despite the broad range of Re_d , Re_D and Re_h , the data points with the same value of Γ_D and S_C but different D/d from these different studies lie in the same wake regimes in figure 5.

equation (Ho & Huerre 1984). It has been shown that the dimensionless spatial growth rate ($-\alpha_i\theta$, i subscript denotes imaginary part) of the perturbation peaks at $f_{KH}^* = f_{KH}\theta/\bar{U} = 0.032$ for the hyperbolic-tangent profile (3.6) (e.g. Monkewitz & Huerre 1982). This f_{KH} is often termed the natural frequency of the mixing layer.

The broadband peaks in the velocity spectra of regime KH all span f_{KH}^* (figure 8). The arithmetic mean value of the lower and upper bounds of the observed KH frequency (f_1^* and f_2^* defined by chosen critical value of $S_{vv}/(S_{vv})_{max}(= 0.2)$, dot-dashed line in figure 8) for these three cases is 0.036 ± 0.004 , fairly consistent with f_{KH}^* . Similar agreement between the experimentally observed broadband peak and the natural KH frequency has been observed in the wake of a single solid cylinder with a permeable wake splitter plate (Cardell 1993) and the transverse shear flow adjacent to an infinitely long array of cylinders (White & Nepf 2007). This agreement supports the conclusion that the broadband peak observed in regime KH (figure 4*i*) is indicative of Kelvin–Helmholtz instability, which generates the coherent vortices seen in figure 4(*g*).

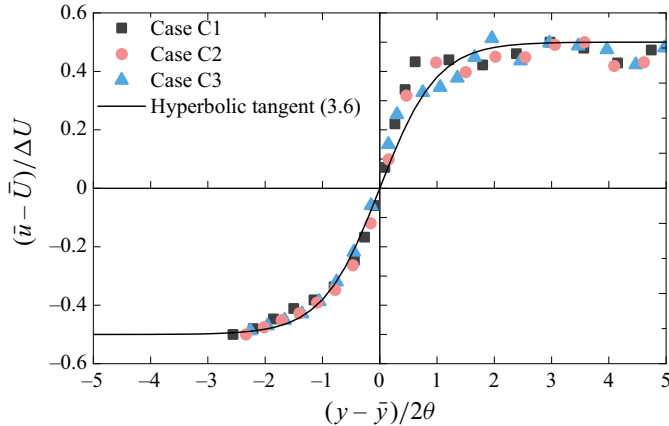


Figure 7. Comparison of measured mean velocity profiles at $x/D = 3$ (all cases in regime KH) to the function presented in (3.6). Here, \bar{y} occurs at $y/D \approx \pm 0.5$ in all cases. The agreement between the measured velocity profiles and the hyperbolic tangent profile of a mixing layer is strong, highlighting the validity of the mixing layer analogy for the array shear layers.

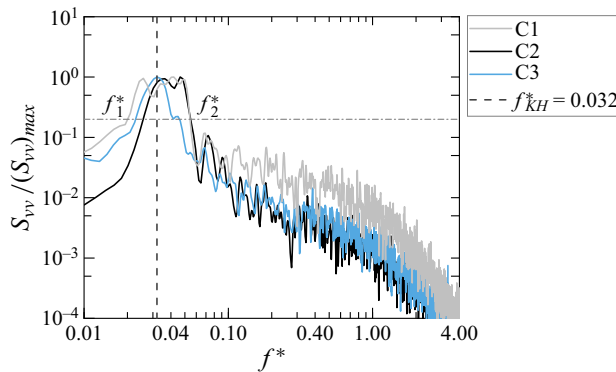


Figure 8. Collapse of spectrum of transverse velocity for three regime KH flows. The power spectral density is normalised by its maximum, and the frequency is normalised as $f^* = f\theta/\bar{U}$. All the spectra were sampled at $y/D = 0.5$ upstream of where two array shear layers merge. The horizontal dashed line represents the chosen critical value of $S_{vv}/(S_{vv})_{max} (= 0.2)$ to determine the upper and lower bounds (f_1^*, f_2^*) of the observed KH frequency. The observed broadband peaks always span the normalised natural frequency ($f_{KH}^* = 0.032$), indicating the occurrence of KH instability in these three cases.

In regime KH, Kelvin–Helmholtz vortices appear to be the first vortex structures observed along the wake. Further downstream, the two array shear layers grow and eventually merge at the centreline (figure 4h), raising the question of whether a von Kármán vortex street forms downstream of the merging point. Dye streaks in regime KH did not manifest distinct regular oscillations as those in regime SS, indicative of the absence of von Kármán vortex street (see supplementary movies 3 and 4). To further confirm this, the spectrogram is evaluated at two locations: upstream (figure 9a,c) and downstream (figure 9b,d) of where the two array shear layers merge. The merging location is identified through dye flow visualisation and the increase in streamwise velocity along the wake centreline according to Zong & Nepf (2012). Upstream of the merging location, energetic high frequencies ($fD/U_\infty > 1$), associated with small vortices shed from the

Wake structure of an array of cylinders in shallow flow

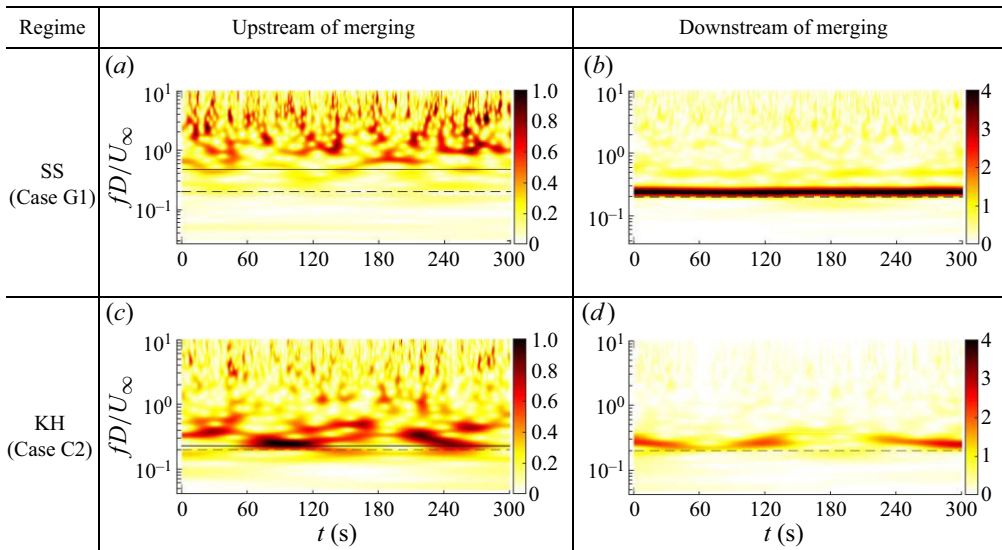


Figure 9. Variation of the velocity spectrum with time. The colour bar represents the amplitude of $v'(t)$ with units of cm s^{-1} . The spectrograms are separated into two groups, i.e. (a,c) upstream and (b,d) downstream of the merging of array shear layers at the centreline. The velocities upstream and downstream of the merging point were sampled at $y/D = 0.5, 0$, respectively. $x/D = (a) 5, (b) 8.5, (c) 1$ and $(d) 5$. The solid lines in panels (a,c) denote the predicted values from linear stability theory ($f_{KH}D/U_\infty$) and the dashed lines in panels (a–d) represent the typical Strouhal number 0.2 of an isolated solid cylinder. Whilst the von Kármán vortex street is characterised by a constant frequency and oscillation amplitude downstream of the merging point in panel (b), the dominant frequencies associated with KH vortices are intermittent over time regardless of location in panels (c,d).

array elements, are detected in regime SS (figure 9a). These are randomly distributed in time and at frequencies much higher than that predicted for the KH instability, i.e. f_{KH} (solid line in figure 9a). Hence, it appears that no KH instability develops within the array shear layers in regime SS. In contrast, lower dominant frequencies ($fD/U_\infty < 0.6$) are observed in regime KH (figure 9c), which are more concentrated in time and closer to the predicted value of KH instability (f_{KH}). If there was von Kármán vortex shedding, the instantaneous oscillation frequency and oscillation amplitude would be expected to remain constant with time (at the vortex shedding frequency) as observed in regime SS flow (see figure 9b). However, the primary frequency around $fD/U_\infty = 0.2$ (dashed line) for regime KH was intermittent over time, with much lower oscillation magnitude relative to regime SS (figure 9d). The intermittency of transverse velocity downstream of the merging point has been confirmed for other regime KH flows (e.g. cases B1, D1, D2, H2) with a quadrupled sample length (1200 s) (spectrogram omitted for simplicity). This is consistent with the observation of an intermittent wake oscillation for a cylinder array with $\Gamma_D \approx 2$ by Ball *et al.* (1996). Therefore, both flow visualisation and wavelet analysis of velocity fluctuations show that in regime KH, the von Kármán vortex street is absent downstream of where the array shear layers merge and start to interact.

In the two-dimensional numerical simulations of flow through a circular array (He *et al.* 2022), it was found that the two array shear layers, containing these large-scale KH vortices, interact with each other to form a secondary vortex street further downstream of the merging point. This secondary vortex is not visible in figure 4(g) due to the limited wake length visualised in the shallow flume for the large array. To confirm the presence

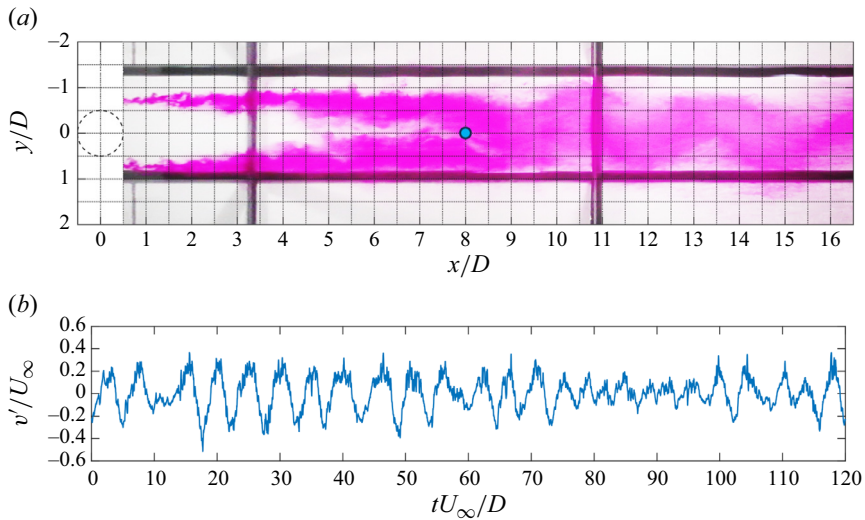


Figure 10. Characteristics of secondary vortex street for case D3* with $(\Gamma_D, S_C) = (8.12, 0.06)$ in regime KH. (a) Instantaneous wake structure; (b) the time history of v' sampled at $(x/D, y/D) = (8, 0)$ (located at the blue dot in panel a). Although the secondary vortex street in panel (a) is similar to the von Kármán vortex street in figure 4(a) in terms of meandering form, the secondary vortex street is generated irregularly over time as indicated by discontinuous oscillations in panel (b).

of secondary vortex street in shallow flow for regime KH, a small array with $D/d = 24$ is created, allowing to examine the wake structure with length up to $16D$ downstream of the array.

Figure 10(a) shows that the two array shear layers grow, driven by KH instability, to merge and interact at $x/D \approx 8$, forming a secondary vortex street downstream. Although the secondary vortex street is similar to the von Kármán vortex street in regimes SS and VS in terms of the meandering form (comparing figure 10a with figures 4a,d), the generation of secondary vortex street is very irregular with time. This is evidenced by figure 10(b) where the large-scale oscillations of transverse velocity (such as an example at $(x/D, y/D) = (8, 0)$), indicating generation of the secondary vortex street, occur in the time range of $tU_\infty/D \approx 15$ – 75 but cease in the range of 75 – 100 .

Physically, the secondary vortex street is a result of interaction between two rows of KH vortices at either side of the array. These KH vortices in each array shear layer are, however, generated irregularly over time, as indicated by irregularity of oscillations in time histories of v'/U_∞ upstream of the merging point ($x/D = 2, 6$, not shown). In the two-dimensional flow (He *et al.* 2022), the irregularly generated KH vortices will merge randomly within either array shear layer, before interacting with merged KH vortices in the other array shear layer. The irregularity of generation of KH vortices and the random amalgamation of KH vortices are expected to be the reason for the irregularity of the secondary vortex street in shallow flow.

The results in figures 9 and 10 combined with numerical results from He *et al.* (2022) illustrate the fundamental distinction between regimes KH and SS, although the normalised dominant frequency in the two regimes both approach 0.2 in the far wake (see figure 9b,d). This finding may answer the question raised in previous studies (Zong & Nepf 2012; Chang & Constantinescu 2015) as to why a dominant frequency close to the typical Strouhal number of 0.2 can be detected despite the absence of a clear vortex shedding

pattern when the two array shear layers merge and interact. The Strouhal number of ~ 0.2 in regime KH corresponds to the secondary vortex street.

With these distinctive features for regime KH, the evidence for classifying the data points from existing work into regime KH in figure 5 is explained. First, despite the absence of a von Kármán vortex street, the array shear layers have been found to display large-scale undulatory motions (Chang & Constantinescu 2015) (denoted ‘ ∇ ’ in figure 5); second, the two array shear layers eventually merge with the formation of a meandering wake flow downstream instead of vortex shedding (Zong & Nepf 2012) (denoted ‘ \square ’); third, a frequency (fD/U_∞), detected in the array wake, is close to that expected for von Kármán vortex shedding ($\Gamma_D \approx 0.2$) (Zong & Nepf 2012; Chang & Constantinescu 2015). It appears that the large-scale undulatory motions and the characteristic frequency ($fD/U_\infty \approx 0.2$) are consistent with the KH instability, and a secondary vortex street may be responsible for the wake meandering downstream of merging point. In addition to these cases, there is one case (‘ Δ ’ near $\Gamma_D = 2.2$) from figure 10(c) of Nicolle & Eames (2011), for which two rows of coherent structures are formed without von Kármán vortex shedding and the two rows then interact downstream to develop a vortex street. It appears that this case, originally classified as regime CI by Nicolle & Eames (2011), is also consistent with regime KH. These cases from previous studies are therefore tentatively classified into regime KH (red hollow squares in figure 5).

Regime KH was also observed in the wake of other porous obstacle systems, for example, the wake of a porous plate (Huang & Keffer 1996) and a screen cylinder (Sun *et al.* 2021). Fundamentally, the bleeding flow for the system of porous obstacles acts to suppress the interaction of array shear layers. Accordingly, the absolute instability (Huerre & Monkewitz 1985), manifested by von Kármán vortex shedding, is suppressed. Following this, flow features associated with the KH instability (convective instability) become dominant in the wake.

3.2. Wake flow characteristics

3.2.1. Shear layer growth

As the wake structure is a result of the development of array shear layers (Zong & Nepf 2012), in this section, a comparison of the downstream growth of array shear layers in regimes SS, KH and CI is presented, which helps to reveal the difference in formation mechanism between the three regimes. Note that in regime VS, array shear layers have limited growth behind the array and are not considered here. The shear layer growth is quantified through transverse profiles of the normalised Reynolds shear stress $-\overline{u'v'}/U_\infty^2$ (figure 11). Edges of the array shear layers where Reynolds shear stress is less than 20% of its maximum in a profile at any streamwise location are marked with red dashed lines.

Focusing on regime SS first, it is evident that the array shear layer grows slowly close to the array, with width increasing from $0.30D$ at $x/D = 1$ to $0.37D$ at $x/D = 3$ (figure 11a). It then experiences rapid growth between $3 < x/D < 5$, with the width almost doubling. As a result, the two shear layers on either side of the array merge at the centreline near $x/D = 5$, which is consistent with the flow visualisation (C_V contour) in figure 4(e). From $x/D = 3$ to 5, the shear layer growth coincides with an increase in the rate of lateral momentum transport across the shear layer, as indicated by an increase in the magnitude of $-\overline{u'v'}/U_\infty^2$. This rapid growth is associated with the formation of the von Kármán vortex street, as evidenced by the non-zero $-\overline{u'v'}/U_\infty^2$ next to the centreline, the rapid increase in the magnitude of $-\overline{u'v'}/U_\infty^2$ along the centreline for $5 < x/D < 8.5$ and vortex shedding starting at $x/D \approx 5$ (see dye streaks in figure 4d).

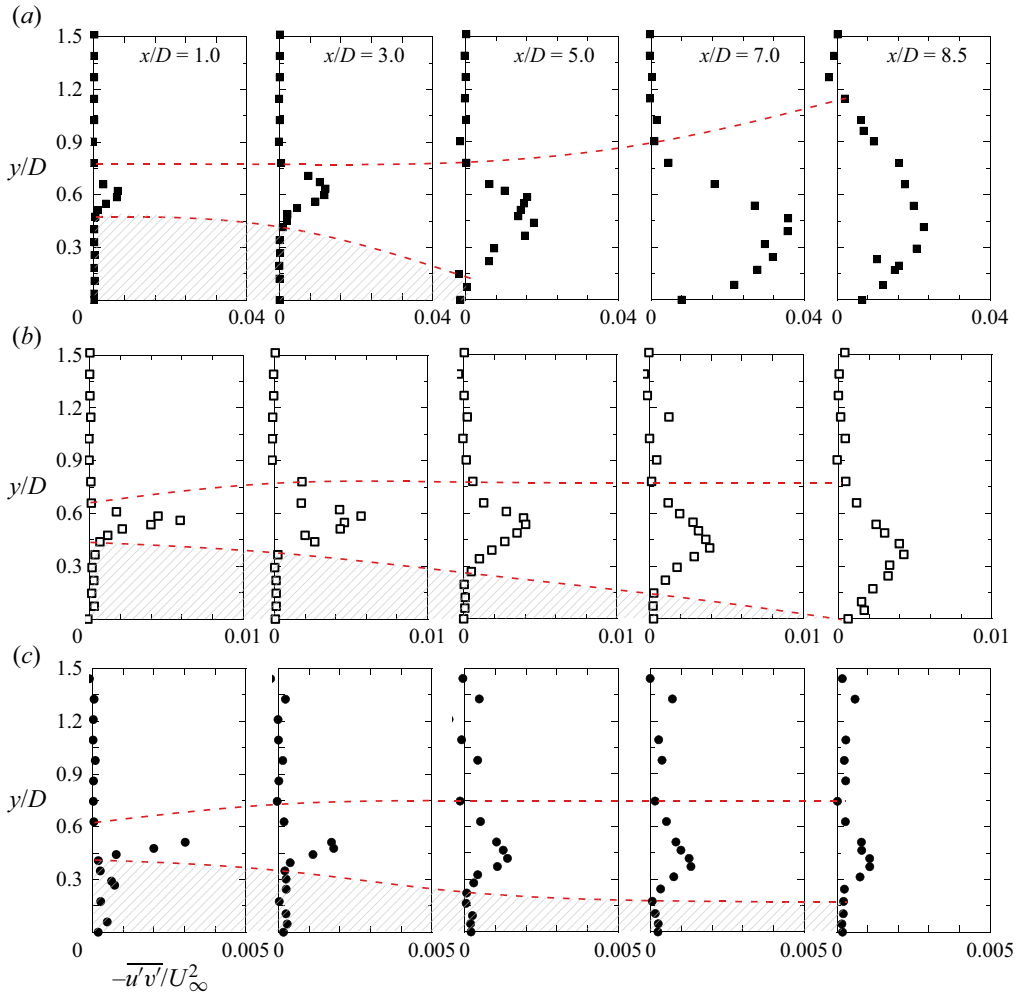


Figure 11. Comparison of the growth of array shear layers in (a) the SS regime (case F1), (b) the KH regime (case C1) and (c) the CI regime (case A1). The red dashed lines mark the edges of shear layers, which are defined by the transverse location where the Reynolds shear stress is less than 20% of the maximum in the profile. Hashed region represents the steady wake region in the field of view. The shear layer growth rate decreases as the wake flow varies from regime SS to KH and to CI.

In contrast to regime SS, the array shear layers in regime KH grow slowly along the wake (figure 11b), indicating that the KH vortices are less efficient at driving shear layer growth. This results in a delayed merging of the two array shear layers at $x/D \approx 8.5$ in regime KH (compare figures 11a and 11b). Again, the linear growth of the shear layers, indicated by velocity measurements, is consistent with that shown by the C_V contours (figure 4h), which indicates merging at the same location ($x/D \approx 8.5$).

Finally, the shear layer evolution for regime CI is different from both regimes SS and KH. The shear layer grows initially, with its width tripled from $x/D = 1$ to 7 (figure 11c). However, the shear layer stops growing further downstream, as shown by the virtually constant shear layer width at $x/D > 7$ (figure 11c). The maximum value of $-\overline{u'v'}/U_\infty^2$ decreases steadily with x/D , suggesting that no instability develops within the array shear layers in regime CI. The magnitude of $-\overline{u'v'}/U_\infty^2$ reduces in regime KH and CI compared

Wake structure of an array of cylinders in shallow flow

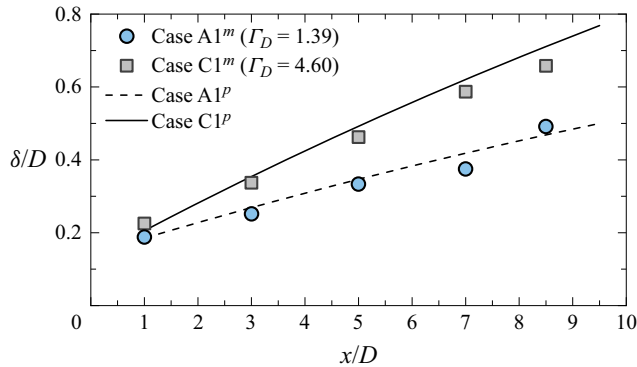


Figure 12. Agreement between the measured and modelled (by (3.9)) development of array shear layer for the cases A1 (regime CI) and C1 (regime KH) both at $S_C = 0.04$. Superscripts 'm' and 'p' represents measurements and predictions, respectively.

with SS (figure 11a–c), indicating a decreasing trend in the rate of turbulent lateral momentum transport as flow varies from regime SS to CI. This is further indicative of increasingly stabilised wake flow.

Despite the differences, the shear layers preferentially grow towards the centreline rather than into the diverted flow in regimes SS and KH, as seen from the expansion of two edges in each flow (figure 11a,b). In other words, the shear layer tends to grow into the low-velocity stream rather than the high-velocity stream, which is consistent with plane mixing layers in both vertically unbounded (Champagne, Pao & Wygnanski 1976) and shallow (van Prooijen & Uijttewaai 2002) flows.

The development of array shear layers as predicted by an existing analytical model is in good agreement with the measurements (see figure 12). The model used to predict the shear layer width $\delta(x)$ was developed based on integration of the shallow water equations both for high- and low-velocity sides of a mixing layer (van Prooijen & Uijttewaai 2002; Van Prooijen 2004) and can be expressed by

$$\frac{\delta(x)}{D} = \gamma \frac{\Delta U}{\bar{U}} \frac{1}{S_C} \left(1 - \exp\left(-S_C \frac{x}{D}\right) \right) + \frac{\delta_0}{D}, \quad (3.9)$$

where γ is the entrainment coefficient for vertically unbounded flow with an empirical value of $\gamma = 0.085$, and δ_0 is initial width of the mixing layer and is approximately $\delta_0 = h$.

Figure 12 shows that with increasing flow blockage parameter, the measured shear layer grows faster. The measured widths of array shear layer agree with those predicted by (3.9), with the root mean squared error less than 3% along the array shear layer for the two cases. This demonstrates the applicability of the analytical model developed based on one single mixing layer to the shear layers generated at either side of the array upstream of where the two shear layers interact.

3.2.2. Steady wake region

As discussed in § 1, the existence and extent of the steady wake region has practical implications for aquatic vegetated systems (e.g. Chen *et al.* 2012; Follett & Nepf 2012). An understanding of its occurrence and streamwise extent L is therefore practically critical and contributes to fully defining shallow wakes. Given that $L = 0$ in regime VS and $L = \infty$ in regime CI, the steady wake region length is only defined for regimes SS and KH.

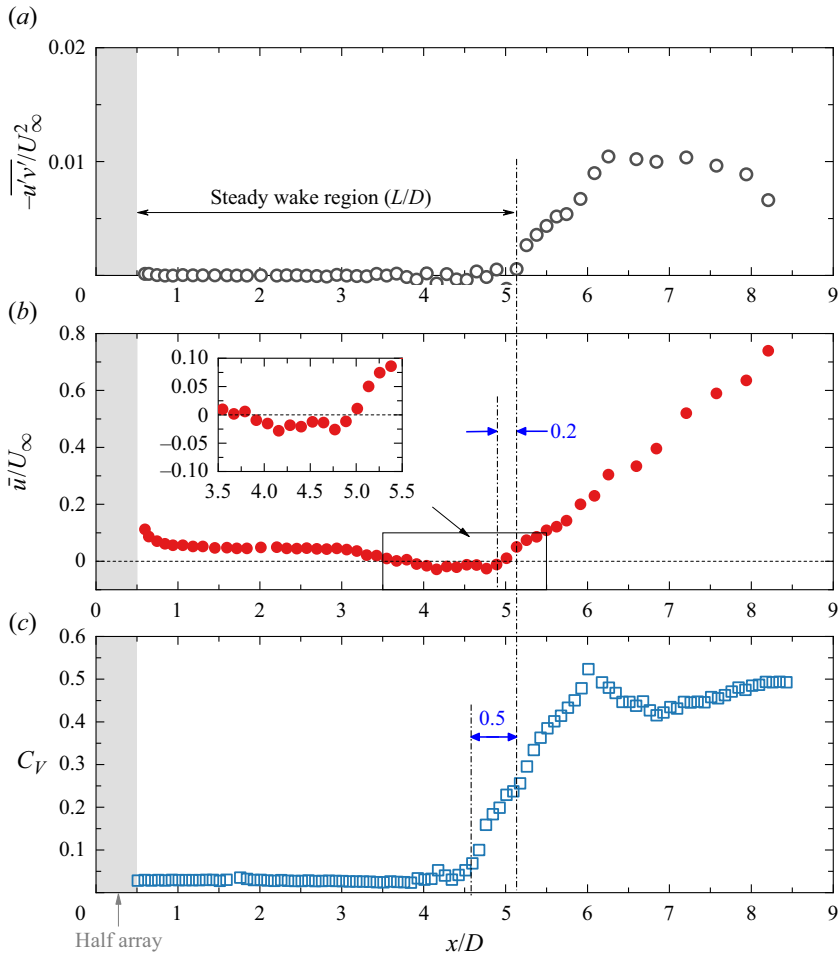


Figure 13. Comparison between the streamwise variations of (a) normalised Reynolds shear stress $-\overline{u'v'}/U_\infty^2$, (b) normalised mean streamwise velocity \bar{u}/U_∞ and (c) coefficient of variation C_V for a regime SS flow (case F1). All the data points in panels (a–c) were sampled along the line of $y/D = 0.05$. The end of the steady wake region is identified as the points where values of $-\overline{u'v'}/U_\infty^2$, \bar{u}/U_∞ and C_V start to increase in the streamwise direction.

Conventionally, L represents the distance along the centreline from the array to the point where the two array shear layers merge (Zong & Nepf 2012). There are two existing methods to quantify L (Zong & Nepf 2012). One is based on velocity measurements as the distance along the centreline from the array to the point where the streamwise velocity starts to increase. The second is based on dye flow visualisation as the distance from the array to the point where dye streaks emerging from either side of the array merge together at the centreline. Here, it is proposed that the first point of non-zero lateral turbulent momentum transport along the centreline also provides a robust description of steady wake region length.

The three techniques above agree reasonably with each other in the estimation of L . First, it is seen that the normalised Reynolds shear stress remains zero ($-\overline{u'v'}/U_\infty^2 < 0.001$) until $x/D = 5.1$ and then starts to increase rapidly (figure 13a). Note that the Reynolds shear stress profile was sampled along the line of $y/D = 0.05$, which was slightly shifted

Wake structure of an array of cylinders in shallow flow

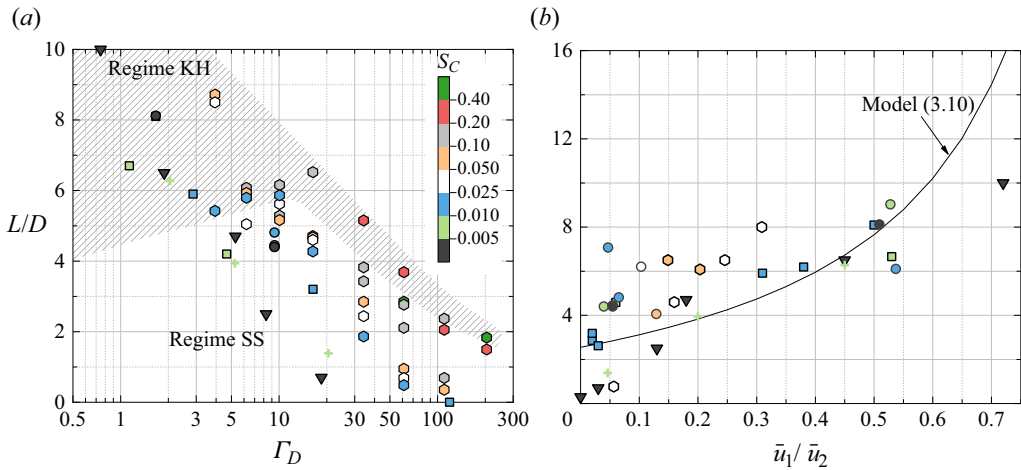


Figure 14. (a) Variation of the steady region length L as a function of Γ_D and S_C . Hexagons, the present study; symbols denoting other studies refer to figure 5. Cases in regime KH are in the hashed region; (b) the comparison of measured values of L with the predictions by (3.10). Some cases in panel (a) are not shown in panel (b) due to lack of velocity measurements for these cases. The steady region length generally increases with increasing S_C in panel (a) and is largely underpredicted by (3.10) in panel (b), highlighting the role of shallowness in controlling shear layer growth.

outwards from the centreline where the Reynolds shear stress is always zero due to its anti-symmetry about the centreline. Since the steady wake region is characterised by nearly zero Reynolds shear stress (hashed region in figure 11), the profile of $-\overline{u'v'}/U_\infty^2$ gives L equal to $4.6D$. Figure 13(b) shows that the streamwise velocity \bar{u}/U_∞ first decreases slightly along the line of $y/D=0.05$ and then remains at $\sim 0.05U_\infty$ until the formation of a recirculation bubble between $4.0 < x/D < 4.9$; the extent of the recirculation bubble is defined as the region where $\bar{u}/U_\infty < 0$ (see the inset of figure 13b), following Zong & Nepf (2012). Further downstream, the streamwise velocity continuously increases presumably due to the momentum transport to the centreline induced by the vortex street. The identification based on \bar{u}/U_∞ gives L equal to $4.4D$. Finally, the coefficient of colour variation (C_V) shows a similar variation with x/D to $-\overline{u'v'}/U_\infty^2$ in figure 13(c). The C_V remains almost zero in the near wake and then increases sharply from $x/D=4.6$, which gives $L=4.1D$. Therefore, the L values estimated by the profile $-\overline{u'v'}/U_\infty^2$, \bar{u}/U_∞ and C_V along the wake centreline are reasonably consistent. Given that velocity measurements were conducted for only some cases in this study, estimation of L based on flow visualisation (C_V) is employed across the whole testing parameter space.

The measured length L combined with observations from existing work indicate that the length generally increases with a decrease of Γ_D and an increase of S_C (figure 14a). However, the L values of the present study (hexagons) are larger than those of previous studies for a given Γ_D as the flows in this study are shallower (larger S_C) than others, highlighting the role of shallowness in modifying the wake structure. The measured L combined with that from previous work is generally decreased as the wake flow transits from regime KH (hashed region) to SS, which means that regimes KH and SS can be reasonably differentiated by L .

The entrainment theory model developed by Zong & Nepf (2012) predicts that the steady wake region has a length

$$L = \frac{D/4}{S_\delta} \left[\frac{1 + \bar{u}_1/\bar{u}_2}{1 - \bar{u}_1/\bar{u}_2} \right], \quad (3.10)$$

where S_δ is a constant empirical entrainment coefficient (0.098) in the absence of shallowness over a wide range of \bar{u}_1/\bar{u}_2 (Champagne *et al.* 1976; Zong & Nepf 2012). It is seen here that (3.10) may underpredict L (figure 14*b*) due most likely to the influence of bed friction. In shallow flow, bed friction has been found to be capable of increasingly inhibiting the shear layer growth downstream (van Prooijen & Uijttewaal 2002), leading to delayed merging of the array shear layers and hence longer steady wake regions. This explains the discrepancy between the measurements and model predictions in figure 14(*b*).

4. Discussion

4.1. Physical mechanisms causing changes in wake structure

In § 3, it has been shown that different wake regimes occur as a result of variation of either Γ_D or S_C . Underlying physical mechanisms associated with the changes in wake structure caused by these two governing parameters will be discussed in the following subsections.

4.1.1. Influence of Γ_D on wake structure

The mechanism of wake transition along the horizontal axis (Γ_D) of figure 5 is considered first. It is shown in figure 5 that the increase of Γ_D leads to increasingly unstable wake associated with generating vortex structures in more coherence. This destabilising influence of Γ_D is associated with its influence on the bleeding flow through the array, as discussed in § 1. Given the interdependent relationship between the stabilising influence of Γ_D and the bleeding flow, the relationship between Γ_D and the bleeding velocity \bar{u}_b/U_∞ (measured at $(x/D, y/D) \approx (0.5, 0)$) is investigated in figure 15. Data from previous studies are also compiled in figure 15. The bleeding velocity is shown to generally decrease with increasing Γ_D . The reduced bleeding velocity imposes less stabilisation on the wake development (Nicolle & Eames 2011; Chang & Constantinescu 2015). Therefore, the wake flow becomes more receptive to instability and will transition into a more unstable regime with the increase of Γ_D .

4.1.2. Influence of S_C on wake structure

The mechanism of the wake structure transition along the vertical axis (S_C) of figure 5 is now considered. The stabilising effects of S_C in the array wake include two parts: (i) suppression of wake instabilities in the far wake; and (ii) secondary influence on the bleeding flow that stabilises the wake.

The primary effect (i) is demonstrated by examining streamwise evolution of velocity and Reynolds shear stress profiles in two characteristic flows with the same value of Γ_D but different values of S_C ; the flows are in the KH and CI wake regimes, respectively. The two flows ($S_C = 0.06, 0.17$) have near-identical velocity profiles in the near wake ($x/D = 1$) (figure 16*a*), indicating similar values of the bleeding velocity and initial transverse shear. However, the evolution of the array shear layer downstream for the two flows is very different. Specifically, as the wake evolves from $x/D = 1$ to 8.5 at low S_C , the local maximum of $-\overline{u'v'}/U_\infty^2$ increases significantly and shifts towards the wake centreline (figure 16*b,c*). The dominant contribution to the Reynolds shear stress in this flow is

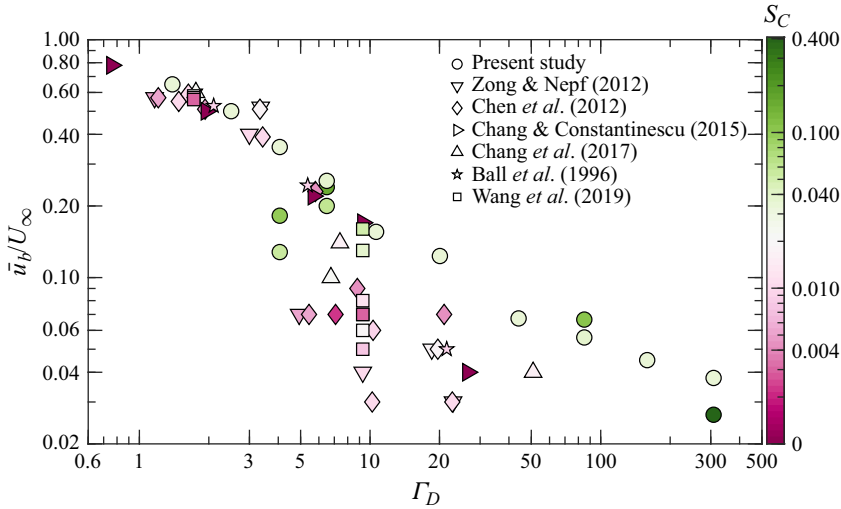


Figure 15. Variation of normalised bleeding velocity \bar{u}_b/U_∞ with Γ_D . While the bleeding velocity is chiefly controlled by, and decreases with, Γ_D , there is a secondary influence of S_C .

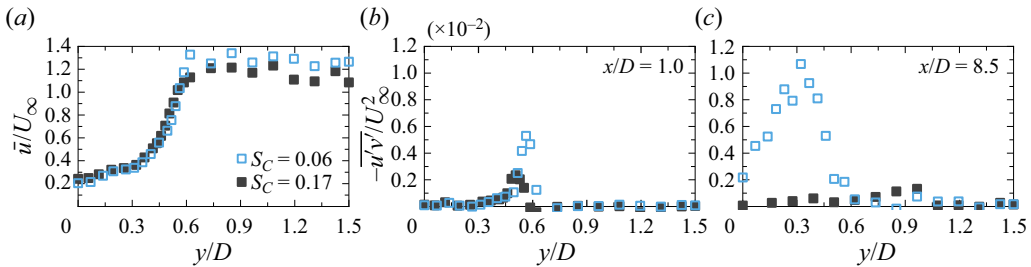


Figure 16. Stabilising effects of S_C on wake instability in two flows (cases D2, D3) at the same Γ_D ($= 6.5$) but different S_C ($= 0.06, 0.17$). The velocity profiles shown in panel (a) were sampled at $x/D = 1$ and the Reynolds shear stress profiles are shown for $x/D = 1$ in panel (b) and 8.5 in panel (c). Hollow and solid squares in panels (a, b, c) denote the cases with $S_C = 0.06$ (regime KH), 0.17 (regime CI), respectively. The wake instability is growing (from panel b to panel c) within array shear layers for the regime KH flow with low $S_C = 0.06$ but is stabilised for the regime CI flow with high $S_C = 0.17$ despite the same bleeding flow for the two cases in panel (a).

the KH vortices, as seen from the time histories of u' and v' . Therefore, the increase in peak values of $-\overline{u'v'}/U_\infty^2$ suggests a growing wake instability within the array shear layers, as observed in the flow visualisation (see supplementary movie 4). In contrast, at higher S_C , the primary peak observed at $x/D = 1$ (figure 16b) does not increase and does not shift towards the wake centreline when moving downstream to $x/D = 8.5$ (figure 16c). The $-\overline{u'v'}/U_\infty^2$ value is almost zero in the range $0 < x/D < 0.6$ at $x/D = 8.5$ (figure 16c), which indicates that u' and v' are nearly non-correlated. Clearly, the lateral momentum transport in the array shear layers and hence wake instability are suppressed downstream. The contrast in the downstream evolution of array shear layers demonstrates that with increasing S_C , the wake flow is progressively stabilised.

The stabilising effect of S_C on the wake instability can be interpreted with reference to the budget of turbulent kinetic energy (TKE) in shear flows. This turbulent kinetic

energy equation has been proposed for a single mixing layer in shallow water by Chu *et al.* (1991) as

$$\frac{\partial k}{\partial t} + \bar{u} \frac{\partial k}{\partial x} = - \underbrace{\left(\bar{u}' \frac{\partial p'}{\partial x} + \bar{v}' \frac{\partial p'}{\partial y} \right)}_{\text{I}} - \underbrace{\bar{u}' \bar{v}' \frac{\partial \bar{u}}{\partial y}}_{\text{II}} - \underbrace{\frac{C_f \bar{u}}{2h} \left[2\bar{u}'^2 + \bar{v}'^2 \right]}_{\text{III}}, \quad (4.1)$$

where $k = (1/2)(\bar{u}'^2 + \bar{v}'^2)$ is the TKE and p' is the fluctuating component of pressure. The first term (I) on the right-hand-side of (4.1) is the pressure-strain term which represents the redistribution of TKE by velocity and pressure fluctuations; the production term (II) represents the rate of TKE extracted from the mean flow by the action of Reynolds stresses and the extracted TKE drives the growth of shear layers; the dissipation term (III) represents the rate of dissipation of TKE by the bed friction. The stabilising influence of bed friction on the shear layer growth can be quantified by the ratio between the production (II) and dissipation (III) terms, which defines the well-known bed friction number:

$$S^* = \frac{C_f \bar{U}}{2h U_y}, \quad (4.2)$$

where U_y is the maximum velocity gradient across the shear layer. A higher bed friction number results in a stronger stabilising influence of the bed friction on the transverse flow motion, a result of wake instability. The wake instability would be suppressed if dissipation is countered exactly by production, that is, $S^* = 1$. Equation (4.2) can be scaled using of following characteristic values:

$$U_y \sim \frac{U_\infty}{D}, \quad \bar{U} \sim \frac{U_\infty}{2}. \quad (4.3a,b)$$

The scaled equation gives exactly the wake stability parameter S_C . This wake stability parameter has also been derived from the shallow water stability equation that describes the influence of bed friction on the development of instability in the wake of an isolated cylinder (Chen & Jirka 1997). Shallow flow through an array of cylinders is somewhere between the mixing layer and the single cylinder wake in shallow water. This explains the stabilising effects of S_C .

In addition to inhibiting wake instabilities in the far wake, the influence of S_C is also seen through its secondary influence on bleeding flow approximately in the range $\Gamma_D = 3\text{--}50$ (figure 15). In this intermediate range, the bleeding velocity is generally increased with increasing S_C . It can be increased by an order of magnitude as S_C increases from 0.01 to 0.1. This general increasing trend of bleeding velocity can be interpreted with the momentum balance. The pressure gradient is balanced by the bed shear in the diverted flow (Rominger & Nepf 2011). The increase of S_C , equivalently bed shear, will retard the diverted flow and hence force more flow to pass through the array due to continuity (Creed *et al.* 2017). At some typical S_C values, the bleeding velocity also reduces with an increase in S_C . The data of the present study (e.g. $\Gamma_D = 3.9$) and Wang *et al.* (2019) (e.g. $\Gamma_D = 9.4$) presented in figure 15 support this finding. This indicates that the variation of bleeding velocity with S_C is not completely monotonic and the influence of bed friction on bleeding velocity is nonlinear. Overall, whilst the flow blockage parameter acts as the chief controller of bleeding velocity across the practical parameter range (figure 15), the wake stability parameter influences the wake development downstream of the array (figure 16) and, to a lesser extent, influences the bleeding velocity (figure 15).

These mechanisms for wake transitions associated with Γ_D and S_C are consistent with (3.9) that describes the growth of a shear layer in shallow flow. Equation (3.9) explicitly describes the stabilising influence of S_C and implicitly reflects on the destabilising influence of Γ_D through $\Delta U/\bar{U}$ since the bleeding velocity is a function of Γ_D and S_C in (3.4). The occurrence of vortex streets (secondary vortex street in regime KH, von Kármán vortex street in regimes SS, VS) can be considered as a result of two array shear layers growing onto the wake centreline and interacting. Equation (3.9) indicates that for a constant value of $\Delta U/\bar{U}$, a higher S_C value results in a lower growth rate of the shear layer. With slower growth, it takes a longer distance for two array shear layers to grow onto the wake centreline and interact to form a vortex street (i.e. increasingly inhibited instabilities). This is how the increase of S_C contributes to suppressing the wake instabilities. In comparison to this, as Γ_D increases, the bleeding velocity is decreased and hence the term $\Delta U/\bar{U}$ is increased, which leads to higher growth rate. This shows how the increases of Γ_D favours the development of wake instabilities through changing the bleeding velocity.

The nonlinear variation of bleeding velocity with wake stability parameter may be associated with the limitation of the use of flow blockage parameter to quantify the dimensionless array-induced blockage to the flow. In practice, the limitation is that the average drag coefficient of individual elements C_d embedded in Γ_D will normally not be known *a priori*. In the present study, the average drag coefficient is predicted by the approach of He *et al.* (2023). As d/h of the present study is in the range of 0.1–1, the individual elements within the array are subjected to moderately shallow conditions according to Zeng & Constantinescu (2017). Therefore, the bed friction not only influences the array-scale wake but may also stabilise the wake of individual elements. The wake stabilisation tends to increase the drag coefficient for an isolated solid cylinder (e.g. Sumer & Fredsøe 1997). However, the influence of bed friction on C_d is not considered in the predictive approach of C_d by He *et al.* (2023), such that increasing S_C may generate a greater-than-predicted value of C_d . Therefore, it is difficult to keep the flow blockage parameter truly constant while varying the wake stability parameter. With increasing S_C , the increase of element drag counteracts the increase of bed shear in adjusting the bleeding velocity. Depending on the balance between the two counteracting effects, an increase of S_C can either increase or decrease the bleeding flow, i.e. nonlinear variation.

When decreasing water depth to increase S_C , the incident flow will transition from the turbulent to laminar state. This state transition may lead to additional stabilisation influence on the wake structure on the top of shallowness effects (bed friction, vertical dimension constraint). In the laboratory experiments, it is observed that the turbulent diffusion of dye streaks injected in the empty flume disappears when $h \leq 1.5$ cm ($S_C > 0.24$). This suggests that this transition occurs around $Re_h = 1500$, which is consistent with the findings of Chen & Jirka (1995). Therefore, the stabilising influence on the wake structure with increasing S_C above 0.24 in the present study is not only due to shallowness effects, but is also related to the transition into laminar incident flow.

In addition to the flow blockage and wake stability parameters, there are other factors that could play a secondary role to influence the wake structures, such as the relative bottom boundary layer thickness (δ_t/D where δ_t is the turbulent boundary layer thickness in the ambient flow) (Taddei, Manes & Ganapathisubramani 2016), the laboratory channel wall blockage ratio (D/W) (Creed *et al.* 2017) and the arrangement of individual elements within an array (Gijón Mancheño *et al.* 2021). Further work is recommended to explore the influence of these additional factors on wake characteristics.

4.2. Comparison between the cylinder array and an isolated cylinder

The wake structure behind an isolated cylinder is well understood in the literature (e.g. Sumer & Fredsøe 1997). This classical scenario sets the limit for the cylinder array when the array becomes very solid ($\Gamma_D = \infty$, with the same diameter as the array). Comparing the wake structure between the array and the isolated cylinder can help to create a link between results of the cylinder array and well-established knowledge about the isolated cylinder and interpret the array wake structure.

While there is some similarity of wake structure between the cylinder array and the isolated solid cylinder, flow through an array of cylinders is distinct due to two physical reasons: (i) a portion of incoming flow passes through gaps between individual cylinders (bleeding flow) into the array-scale wake; (ii) element-scale vortices shed from individual cylinders within the array significantly influence the array-scale vortices forming behind the array. As a result, the array-scale wake characteristics behind the cylinder array are different compared with the isolated solid cylinder, as detailed below.

The presence of bleeding flow contributes to forming a region of steady flow (with positive streamwise velocity) behind the array, which generates three characteristic wake regimes, namely, coupled individual wake (CI), Kelvin–Helmholtz instability wake (KH) and ‘steady + shedding’ wake (SS) (as detailed in § 3.1.1). These three regimes are, however, absent for the isolated solid cylinder. Figure 15 shows that when the flow blockage of the cylinder array becomes very large, the bleeding flow would approach zero. The cylinder array is then characterised by a ‘vortex street’ wake similar to the solid body is (see the ‘vortex street’ wake (VS) in the regime chart in figure 5).

Despite similarity of wake form in regime VS, the presence of bleeding flow leads to a wider flow separation angle to the array perimeter and weaker shear layer for the cylinder array relative to the solid cylinder. Figure 17 presents the comparison of Reynolds shear stress profile (at $x/D = 1$) between the cylinder array and the isolated cylinder in the same regime VS. The maximum of $-\overline{u'v'}/U_\infty^2$ for the solid cylinder is shown to be approximately 1.4 times larger than that of the cylinder array. This suggests that the array shear layers are weaker than the shear layers separated from the solid cylinder, highlighting the influence of bleeding flow in reducing the array shear layer strength for the cylinder array. The Reynolds shear stress peaks at $y/D \approx 0.4$ for the cylinder array, in contrast to $y/D \approx 0.2$ for the solid cylinder. As this peak location represents the time mean location of oscillating shear layer, the larger y/D value indicates that the array shear layers have a wider separation angle to the array perimeter in comparison to the separated shear layers of the solid cylinder. This is because the bleeding flow exiting either side of the array pushes the shear layer away from the array perimeter (Taddei *et al.* 2016). A similar finding of a wider separation angle was presented by Nicolle & Eames (2011) through flow visualisation.

The bleeding flow also makes the development of KH instability in the array wake different from that in the solid cylinder wake. In the wake of an isolated cylinder, it has been found that the separated shear layers initially develop KH vortices with vortex shedding subsequently generated in the near wake (Prasad & Williamson 1997). That is, KH vortices and von Kármán vortices coexist for the separated shear layers. However, across the parameter space of Γ_D and S_C considered herein, such a coexistence is not observed in the array wake. This is expected to be associated with the bleeding flow reducing the strength of the array shear layers, such that there is not sufficient shear to sustain the vortex shedding after the formation of KH instability vortices within array shear layers. The frequency of KH instability is one order of magnitude larger than that of vortex shedding at $Re_D \sim O(10^4)$ (Prasad & Williamson 1997) for the isolated cylinder. However, spectral peaks in regimes KH, SS and VS in the cylinder array wake explored here have

Wake structure of an array of cylinders in shallow flow

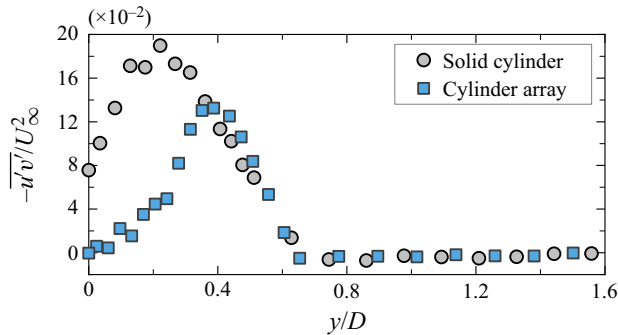


Figure 17. Comparison of profile of Reynolds shear stress at $x/D = 1$ between a cylinder array and an isolated cylinder in regime VS. $(\Gamma_D, S_C) = (308.5, 0.04)$ for the cylinder array and $(\Gamma_D, S_C) = (\infty, 0.04)$ for the solid cylinder. The array has the same diameter as the solid cylinder ($D = 41.3$ cm). The peak value of $-\overline{u'v'}/U_\infty^2$ for the cylinder array is much lower and the peak location is far away from the wake centreline ($y/D = 0$), suggesting weaker array shear layers and wider separation angle of array shear layers in comparison to these of the isolated solid cylinder.

similar magnitudes and normalised frequencies ($fD/U_\infty \approx 0.2$, similar to an isolated cylinder) (see figure 4*c,f,i*). As the KH instability frequency is inversely proportional to the momentum thickness θ , the contrast in the KH instability frequency between the cylinder array and the isolated solid cylinder is due to the difference in the momentum thickness between them. The momentum thickness is of the order of $\theta/D \sim O(10^{-2})$ in the near wake of a cylinder array with the presence of bleeding flow, which is just one order of magnitude larger than that for the isolated cylinder (figure 15 of Prasad & Williamson 1997). This explains the difference in the KH instability frequency between the two systems.

The threshold of wake transition for the cylinder array is also one order of magnitude lower than that of the solid cylinder due to the presence of bleeding flow. For an isolated solid cylinder ($\Gamma_D = \infty$), the critical value of S_C for the shallowness influence to cause wake transition is 0.2 according to Chen & Jirka (1995). However, for an array of cylinders considered in the present study, the transition into a relatively stable wake can occur even at $S_C = 0.01$ (see figure 5), which is one order of magnitude lower than that for the isolated cylinder. This highlights the importance of investigating the shallowness influence on the wake structure behind an array of cylinders. Instabilities in the array wake are much easier to stabilise due to shallowness than those in the single cylinder wake due to the additional stabilising effects of bleeding flow. This means that a lower S_C value is needed for the wake transition into a relatively stabilised regime for the cylinder array, in comparison to that of the solid cylinder.

The element-scale vortices shed from individual cylinders have several impacts on the array-scale wake according to literature and experiments in this study. First, the element-scale vortices merge together to generate strong turbulence in the near wake of a cylinder array. This is demonstrated by velocity measurements where high-frequency velocity fluctuations are observed (not shown here). This was also reported in the existing literature (e.g. Chen *et al.* 2012; Zong & Nepf 2012). Second, in comparison to the solid cylinder, the element-scale vortices from cylinders are advected into the array shear layers, as visualised in our experiments (not shown). This can help trigger the instability of array shear layers (Ball *et al.* 1996). Finally, the element-scale vortices advected into the array shear layers contribute to developing the three dimensionality of the array-scale wake (Chang & Constantinescu 2015). The three dimensionality of the solid cylinder wake is however primarily developed from either an elliptic instability of the primary vortex cores

or the hyperbolic instability of the braid shear layer region (Williamson 1996; Jiang *et al.* 2016).

5. Conclusions

In this paper, a predictive framework for the wake structure behind an array of emergent cylinders is developed based on the dimensionless flow blockage parameter Γ_D and wake stability parameter S_C , over a wide, practical parameter space of $(\Gamma_D, S_C) = (1 \rightarrow \infty, 0-0.5)$. Development of this framework is underpinned by a series of laboratory experiments that use dye flow visualisation and velocity measurements to characterise the wake structure in shallow flow. The controlling influence of Γ_D and S_C on the wake structure is demonstrated as two arrays with the same values of Γ_D and S_C , but different dimensionless array sizes (D/d) display the same wake structure. The dependence of the wake structure on Γ_D and S_C has been demonstrated to be a consequence of (i) the influence of the flow blockage parameter on the bleeding flow that stabilises the wake and (ii) the ability of shallowness to suppress wake instabilities and (to a lesser extent) also influence the bleeding flow.

The framework predicts four wake regimes: (i) the vortex street wake (VS), in which a von Kármán vortex street forms immediately behind the array; (ii) the ‘steady + shedding’ wake (SS), in which a steady wake region occurs behind the array, followed downstream by a von Kármán vortex street; (iii) the Kelvin–Helmholtz instability wake (KH), where large-scale vortices associated with the Kelvin–Helmholtz instability are formed within the array shear layers; and (iv) the coupled individual wake (CI), in which the array wake is dominated by individual wakes of the cylinders within the array and the array shear layers are stabilised. Systems progress in order through regimes (i) \rightarrow (iv) with either decreasing Γ_D or increasing S_C over the parameter space investigated. Flow characteristics for each wake regime are presented. All wake regimes can be distinguished in wake characteristics such as the instantaneous and time-averaged flow fields, transverse velocity oscillations, and the rate of shear layer growth.

Regime KH is a new regime identified in this study. The distinctive feature for regime KH is that a series of Kelvin–Helmholtz vortices growing downstream is observed within array shear layers. Accordingly, there is a broadband peak in the spectrum of transverse velocity, in contrast to the sharp peak observed for regime SS and the absence of dominant peaks for regime CI; the dominant oscillation frequencies of transverse velocity in regime KH are intermittent over time. Further downstream, the two rows of KH vortices respectively in two array shear layers interact with each other to form a second vortex street.

Shallowness suppresses the downstream growth of array shear layers, as it does to a single mixing layer in shallow water. As a result, the analytical model developed based on the single plane mixing layer by Van Prooijen (2004) predicts well the development of array shear layers. In contrast, the model of entrainment theory (Zong & Nepf 2012) without considering the shallowness effects underpredicts the length of the steady wake region for shallow flow. The steady wake region length generally increases with S_C .

Prediction of wake structure for an array of obstacles using this developed framework requires only the knowledge of the array geometry and the depth and velocity of incident flow (to calculate Γ_D and S_C). The predictive framework and accompanying results of flow characteristics allow for a more complete understanding of the influence of array density and flow depth on the mean and turbulent flow fields behind obstacle arrays. Across a range of natural and engineered systems, they can serve as the basis for describing variation in

the downstream length over which there is steady flow, the scale and strength of coherent structures in the wake, and rates of lateral mass transport.

Supplementary movies. Supplementary movies are available at <https://doi.org/10.1017/jfm.2024.338>.

Acknowledgements. F.H. would like to acknowledge the support from the Australian Government and the University of Western Australia by providing RTP and UPA scholarships for a doctoral degree. We are grateful for helpful suggestions from Dr S.U. Villota at the University of Melbourne on ADV velocity measurements.

Funding. This research received no specific grant from any funding agency, commercial or not-for-profit sectors.

Declaration of interests. The authors report no conflict of interest.

Author ORCIDs.

-  Fei He <https://orcid.org/0000-0001-7364-5641>;
-  Marco Ghisalberti <https://orcid.org/0000-0002-6690-8922>;
-  Hongwei An <https://orcid.org/0000-0002-9082-1405>;
-  Scott Draper <https://orcid.org/0000-0002-4185-0111>;
-  Paul Branson <https://orcid.org/0000-0002-3825-9873>;
-  Chengjiao Ren <https://orcid.org/0000-0001-8342-6522>;
-  Liang Cheng <https://orcid.org/0000-0002-1640-542X>.

REFERENCES

- BALL, D., STANSBY, P., ALLISON, N. & STROUHAL 1996 Modelling shallow water flow around pile groups. *Proc. Inst. Civil Engrs-Water Maritime Energy* **118**, 226–236.
- BELCHER, S., JERRAM, N. & HUNT, J. 2003 Adjustment of a turbulent boundary layer to a ‘canopy’ of roughness elements. *J. Fluid Mech.* **488**, 369–398.
- BOULORD, A., MEI, Z., TIAN-HOU, W., XIAO-MING, W. & JIGUET, F. 2012 Reproductive success of the threatened Reed Parrotbill *Paradoxornis heudei* in non-harvested and harvested reedbeds in the Yangtze River estuary, China. *Bird Conserv. Intl* **22**, 339–347.
- CARDELL, G.S. 1993 *Flow Past a Circular Cylinder with a Permeable Wake Splitter Plate*. California Institute of Technology.
- CHAMPAGNE, F., PAO, Y. & WYGNANSKI, I.J. 1976 On the two-dimensional mixing region. *J. Fluid Mech.* **74**, 209–250.
- CHANG, K. & CONSTANTINESCU, G. 2015 Numerical investigation of flow and turbulence structure through and around a circular array of rigid cylinders. *J. Fluid Mech.* **776**, 161–199.
- CHANG, W.-Y., CONSTANTINESCU, G. & TSAI, W.F. 2017 On the flow and coherent structures generated by a circular array of rigid emerged cylinders placed in an open channel with flat and deformed bed. *J. Fluid Mech.* **831**, 1–40.
- CHEN, D. & JIRKA, G.H. 1995 Experimental study of plane turbulent wakes in a shallow water layer. *Fluid Dyn. Res.* **16**, 11–41.
- CHEN, D. & JIRKA, G.H. 1997 Absolute and convective instabilities of plane turbulent wakes in a shallow water layer. *J. Fluid Mech.* **338**, 157–172.
- CHEN, Z., ORTIZ, A., ZONG, L. & NEPF, H. 2012 The wake structure behind a porous obstruction and its implications for deposition near a finite patch of emergent vegetation. *Water Resour. Res.* **48**, 1–12.
- CHOW, V. 1959 *Open-Channel Hydraulics*. McGraw-Hill.
- CHU, V.H., WU, J.H. & KHAYAT, R.E. 1991 Stability of transverse shear flows in shallow open channels. *ASCE J. Hydraul. Engng* **117** (10), 1370–1388.
- COULBOURNE, W. *et al.* 2011 *Coastal Construction Manual, Principles and Practices of Planning, Siting, Designing, Constructing, and Maintaining Residential Buildings in Coastal Areas*. FEMA-US.
- CREED, M., DRAPER, S., NISHINO, T. & BORTHWICK, A. 2017 Flow through a very porous obstacle in a shallow channel. *Proc. R. Soc. A: Math. Phys. Engng Sci.* **473**, 1–17.
- DUARTE, C.M. & SAND-JENSEN, K. 1990 Seagrass colonization: patch formation and patch growth in *Cymodocea nodosa*. *Mar. Ecol. Prog. Ser.* **65**, 193–200.
- EAMES, I., HUNT, J.C.R. & BELCHER, S.E. 2004 Inviscid mean flow through and around groups of bodies. *J. Fluid Mech.* **515**, 371–389.

- FOLLETT, E.M. & NEPF, H.M. 2012 Sediment patterns near a model patch of reedy emergent vegetation. *Geomorphology* **179**, 141–151.
- GARRETT, C. & CUMMINS, P. 2007 The efficiency of a turbine in a tidal channel. *J. Fluid Mech.* **588**, 243.
- GHISALBERTI, M. 2009 Obstructed shear flows: similarities across systems and scales. *J. Fluid Mech.* **641**, 51–61.
- GIJÓN MANCHEÑO, A., JANSEN, W., WINTERWERP, J.C. & UIJTTEWAAL, W.S.J. 2021 Predictive model of bulk drag coefficient for a nature-based structure exposed to currents. *Sci. Rep.* **11**, 1–13.
- GURNELL, A.M., PETTS, G.E., HANNAH, D.M., SMITH, B.P., EDWARDS, P.J., KOLLMANN, J., WARD, J.V. & TOCKNER, K. 2001 Riparian vegetation and island formation along the gravel-bed Fiume Tagliamento, Italy. *Earth Surf. Process. Landf.: J. Brit. Geomorphol. Res. Group* **26**, 31–62.
- HE, F. 2023 Hydrodynamics within and behind a porous obstruction in steady flow. Doctoral thesis thesis, The University of Western Australia.
- HE, F., DRAPER, S., GHISALBERTI, M., AN, H. & BRANSON, P. 2023 Predicting mean flow through an array of cylinders. Authorea Preprints.
- HE, F., DRAPER, S., GHISALBERTI, M., AN, H.W., BRANSON, P., CHENG, L. & REN, C.J. 2022 Wake structure behind porous obstructions in steady current. In *23rd Australasian Fluid Mechanics Conference*, Sydney, Australia.
- HO, C.-M. & HUERRE, P. 1984 Perturbed free shear layers. *Annu. Rev. Fluid Mech.* **16**, 365–422.
- HUANG, Z. & KEFFER, J. 1996 Development of structure within the turbulent wake of a porous body. Part 1. The initial formation region. *J. Fluid Mech.* **329**, 103–115.
- HUERRE, P. & MONKEWITZ, P.A. 1985 Absolute and convective instabilities in free shear layers. *J. Fluid Mech.* **159**, 151–168.
- INGRAM, R.G. & CHU, V.H. 1987 Flow around islands in Rupert Bay: an investigation of the bottom friction effect. *J. Geophys. Res.: Oceans* **92**, 14521–14533.
- JIANG, H., CHENG, L., DRAPER, S., AN, H. & TONG, F. 2016 Three-dimensional direct numerical simulation of wake transitions of a circular cylinder. *J. Fluid Mech.* **801**, 353–391.
- KIM, H.S., NABI, M., KIMURA, I. & SHIMIZU, Y. 2015 Computational modeling of flow and morphodynamics through rigid-emergent vegetation. *Adv. Water Resour.* **84**, 64–86.
- KOTSCHY, K. & ROGERS, K. 2008 Reed clonal characteristics and response to disturbance in a semi-arid river. *Aquat. Bot.* **88**, 47–56.
- MONKEWITZ, P.A. & HUERRE, P. 1982 Influence of the velocity ratio on the spatial instability of mixing layers. *Phys. Fluids* **25**, 1137–1143.
- NEZU, I. & NAKAGAWA, H. 1993 *Turbulence in Open Channels*. IAHR/AIRH Monograph. Balkema.
- NICOLLE, A. & EAMES, I. 2011 Numerical study of flow through and around a circular array of cylinders. *J. Fluid Mech.* **679**, 1–31.
- PRASAD, A. & WILLIAMSON, C.H. 1997 The instability of the shear layer separating from a bluff body. *J. Fluid Mech.* **333**, 375–402.
- VAN PROOIJEN, B.C. 2004 Shallow mixing layers. PhD thesis, Delft University of Technology, Delft, The Netherlands.
- VAN PROOIJEN, B.C. & UIJTTEWAAL, W.S.J. 2002 A linear approach for the evolution of coherent structures in shallow mixing layers. *Phys. Fluids* **14**, 4105–4114.
- ROMINGER, J.T. & NEPF, H.M. 2011 Flow adjustment and interior flow associated with a rectangular porous obstruction. *J. Fluid Mech.* **680**, 636–659.
- SUMER, B.M. & FREDSSØE, J. 1997 *Hydrodynamics around Cylindrical Structures*. World Scientific.
- SUN, C., AZMI, A.M., LEONTINI, J., ZHU, H. & ZHOU, T. 2021 Experimental study on the development of wake vortices behind screen cylinders. *Phys. Fluids* **33**, 085133.
- TADDEI, S., MANES, C. & GANAPATHISUBRAMANI, B. 2016 Characterisation of drag and wake properties of canopy patches immersed in turbulent boundary layers. *J. Fluid Mech.* **798**, 27–49.
- TAKEMURA, T. & TANAKA, N. 2007 Flow structures and drag characteristics of a colony-type emergent roughness model mounted on a flat plate in uniform flow. *Fluid Dyn. Res.* **39**, 694.
- TANINO, Y. & NEPF, H.M. 2008 Laboratory investigation of mean drag in a random array of rigid, emergent cylinders. *ASCE J. Hydraul. Engng* **134**, 34–41.
- WANG, C. & WANG, P. 2007 Hydraulic resistance characteristics of riparian reed zone in river. *J. Hydrol. Engng* **12**, 267–272.
- WANG, J., ZHANG, J., LIANG, D. & GAN, L. 2019 Non-hydrostatic modelling of shallow water flow around a circular array of emergent cylinders. *J. Hydroinformat.* **22** (1), 20–32.
- WHITE, B.L. & NEPF, H.M. 2007 Shear instability and coherent structures in shallow flow adjacent to a porous layer. *J. Fluid Mech.* **593**, 1–32.
- WILLIAMSON, C.H.K. 1996 Three-dimensional wake transition. *J. Fluid Mech.* **328**, 345–407.

Wake structure of an array of cylinders in shallow flow

- WOOD, C.J. 1967 Visualization of an incompressible wake with base bleed. *J. Fluid Mech.* **29**, 259–272.
- ZDRAVKOVICH, M.M. 1997 Flow around circular cylinders. *Fundamentals* **1**, 566–571.
- ZENG, J. & CONSTANTINESCU, G. 2017 Flow and coherent structures around circular cylinders in shallow water. *Phys. Fluids* **29**, 066601.
- ZHANG, J., FAN, X., LIANG, D. & LIU, H. 2019 Numerical investigation of nonlinear wave passing through finite circular array of slender cylinders. *Engng Appl. Comput. Fluid Mech.* **13**, 102–116.
- ZHAO, M., CHENG, L., AN, H. & TONG, F. 2015 Flow and flow-induced vibration of a square array of cylinders in steady currents. *Fluid Dyn. Res.* **47**, 045505.
- ZONG, L. & NEPF, H. 2012 Vortex development behind a finite porous obstruction in a channel. *J. Fluid Mech.* **691**, 368–391.